Heterogeneous Ti3SiC2@C-containing Na2Ti7O15 architecture for high-performance sodium storage at elevated temperatures.

ZOU, G., ZHANG, Q., FERNANDEZ, C., HUANG, G., HUANG, J., PENG, Q.

2017

Heterogeneous Ti₃SiC₂@C-Containing Na₂Ti₇O₁₅ Architecture for High-Performance Sodium Storage at Elevated Temperatures

Guodong Zou,[†] Qingrui Zhang,[‡][iD] Carlos Fernandez,[§] Gang Huang,[‖] Jianyu Huang,[†] and Qiuming Peng*,[†][iD]

[†]State Key Laboratory of Metastable Materials Science and Technology, Yanshan University, Qinhuangdao 066004, China

[‡]Hebei Key Laboratory of Applied Chemistry, School of Environmental and Chemical Engineering, Yanshan University, Qinhuangdao 066004, China

[§]School of Pharmacy and Life Sciences, Robert Gordon University, Aberdeen, AB107GJ, U.K.

[‖]WPI Advanced Institute for Materials Research, Tohoku University, Sendai 980-8577, Japan

Ⓢ *Supporting Information*
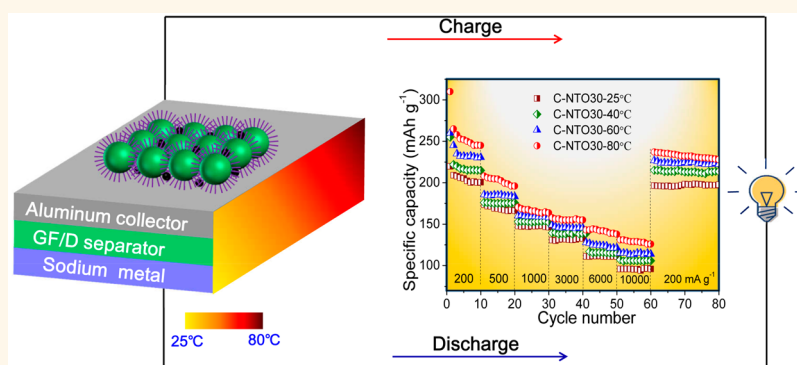
ABSTRACT: Rational design of heterogeneous electrode materials with hierarchical architecture is a potential approach to significantly improve their energy densities. Herein, we report a tailored microwave-assisted synthetic strategy to create heterogeneous hierarchical Ti₃SiC₂@C-containing Na₂Ti₇O₁₅ (MAX@C-NTO) composites as potential anode materials for high-performance sodium storage in a wide temperature range from 25 to 80 °C. This composite delivers first reversible capacities of 230 mAh g⁻¹ at 200 mA g⁻¹ and 149 mAh g⁻¹ at 3000 mA g⁻¹ at 25 °C. A high capacity of ~93 mAh g⁻¹ without any apparent decay even after more than 10 000 cycles is obtained at an ultrahigh current density of 10 000 mA g⁻¹. Moreover, both a high reversible capacity and an ultralong durable stability are achieved below 60 °C for the same composites, wherein a 75.2% capacity retention (~120 mAh g⁻¹ at 10 000 mA g⁻¹) is achieved after 3000 cycles at 60 °C. To the best of our knowledge, both the sodium storage performances and the temperature tolerances outperform those of all the Ti-based sodium storage materials reported so far. The superior sodium storage performances of the as-synthesized composites are attributed to the heterogeneous core−shell architecture, which not only provides fast kinetics by high pseudocapacitance but also prolongs cycling life by preventing particle agglomeration and facilitates the transportation of electrons and sodium ions by large micro/mesopore structure.

KEYWORDS: *pseudocapacitance, electrode, sodium-ion batteries, MAX@C-NTO composite, high rate performance, intercalation*

Demands for rechargeable batteries have been increasing over the past few years due to the great number of applications in electric-powered transportation, stationary energy storage, mobile devices, and smart grids.[1] To meet the practical-economic criteria for large-scale components, sodium-ion batteries (SIBs) have been scheduled due to their beneficial aspects compared to conventional lithium-ion batteries (LIBs) such as their lower cost, abundant raw materials, and environmental friendliness.[2] More importantly, the analogous structure and reaction kinetics of SIBs to those of LIBs are particularly attractive, implying that they may be prepared by the existing setups and related battery technologies of LIBs.[3]
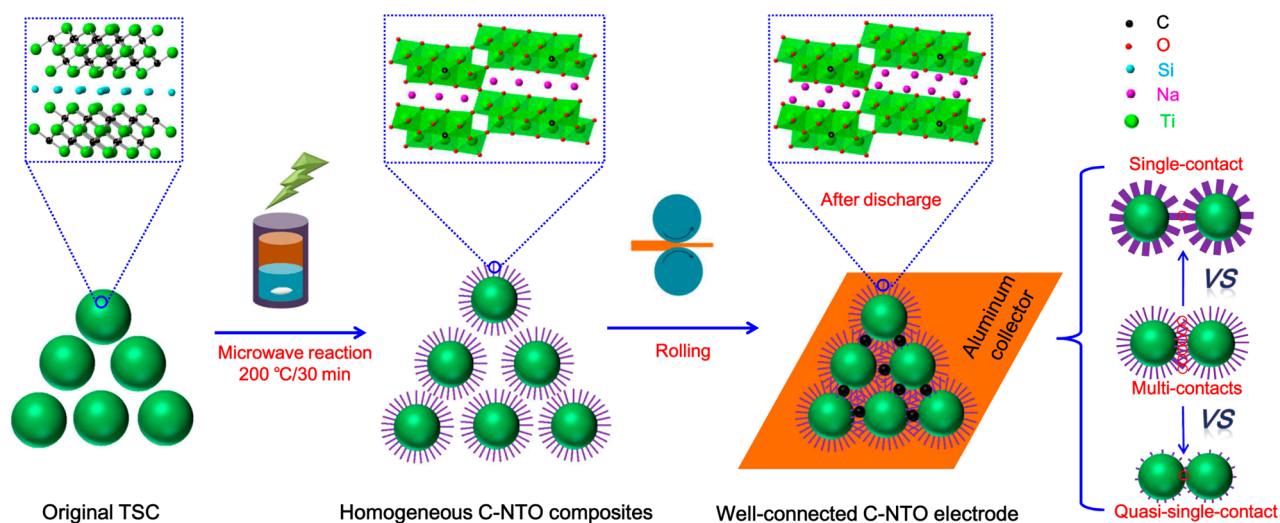
Figure 1. Reaction process and experimental parameters for synthesis of heterogeneous MAX@C-NTO composites. Differing from quasi-single contact and single contact, the multicontacts would provide not only more ions/electrons transfer channels but also higher effective Na intercalation/extraction sites, accounting for good electrochemical performances.

Nevertheless, a major challenge in the SIBs is that they suffer from a lack of suitable electrode materials to reversibly store a considerable amount of large Na ions (1.02 Å) in a fast and stable manner.[4,5] Conventional anode materials such as graphite and Si for SIBs show inferior insertion/extraction kinetics with Na ions,[6,7] resulting in a low capacity and a poor cyclability, as well as inferior rate capability. Alternatives such as organic materials,[8] metal alloys, and metal oxides have been considered to improve sodium storage performances.[9−12] However, the electrical conductivity and the cycle performance of the organic materials need to be further improved before their applications. Large volume fluctuations and sluggish kinetics of alloys restrict their cyclability.[2,13] Intrinsic conductivity of metal oxides is still not satisfactory for long-term running of large-scale energy storage devices, especially at high charge−discharge rates.

In addition, akin to LIBs, operation of SIBs over a wide temperature range is crucial for their industrial applications in various fields. Unfortunately, the performance of SIBs at high temperatures has hardly been considered in contrast to the improvement of capacity and cyclability at room temperature. When SIBs work at high temperatures, movement of Na ions in both the electrolyte and the active material is faster than that at room temperature.[14] Additionally, the liquid electrolyte is more likely to decompose at the interface between the electrolyte and the electrode around the decomposition potential of the electrolyte,[15] which may lead to a rapid exhaustion of electrolyte, an aggregation of Na-hosting materials, and a dramatic degradation of cycle performance. Moreover, although some electrode materials display large capacity and good cyclability, their performances at high temperatures are still unsatisfactory.[16] Hence, a special structural architecture in electrodes with high electrochemical performance in a wide temperature range is desirable for Na storage.

To surpass the limitations of existing electrode materials for NIBs, an electrode with a heterogeneous hierarchical architecture (Figure 1) has been developed, using a MAX as the conductive medium for electrochemical active material. The MAX phase represents a family of compounds with the chemical composition of $M_{n+1}AX_n$ (n = 1, 2, 3), where M stands for an early transition metal, A is assigned to the elements of group IIIA or IVA, and X refers to the C or N component. The MAX phase exhibits higher conductivity ($\sim 10^3$ S/cm) than that of graphite ($\sim 10^{-1}$ S/cm).[17,18] Furthermore, nanosized active materials, for example, titanate, with high capacity can be formed on the surface of the residue MAX phase by in situ phase transformation,[19−21] thus reducing the interface barrier between the MAX phase and the active material. The architecture we have developed in this work has two advantages. First, the residual MAX phase forms an interconnected network after rolling the electrodes, offering excellent electron transport properties and hindering the aggregation of nanosized active materials. Second, the nano-sized active material on the MAX surface has a porous structure, thus facilitating rapid ion transport and mitigating diffusion limitations throughout the entire electrode.[22] This rationally designed composite electrode with compositional and structural superiorities produces interpenetrating electron and ion transport paths that enable inspiring sodium storage performances at high charge−discharge rates at both room temperature and elevated temperatures.

We have used a typical MAX (Ti_3SiC_2) as a model system to fabricate a heterogeneous Ti_3SiC_2@C-containing $Na_2Ti_7O_{15}$ (MAX@C-NTO) composite, wherein the Ti_3SiC_2 in situ transforms into nanosheet C-containing $Na_2Ti_7O_{15}$ on the surface of the MAX after a microwave-hydrothermal treatment. This composite delivers a high rate capacity and an enhanced cycle stability as an anode for SIBs. A capacity of ~ 93 mA h g^{-1} is retained without apparent fading at 25 °C, even after more than 10 000 cycles at a rate of 10 000 mA g^{-1}. More importantly, it offers good high-temperature properties (25−80 °C). For example, a 75.2% capacity retention (~ 120 mA h g^{-1}) is attained at a rate of 10 000 mA g^{-1} after 3000 cycles at 60 °C.

RESULTS AND DISCUSSION

Morphological Features of Heterogeneous Composites. According to the heat-pressure sintering method for Ti_3AlC_2 reported previously by our group,[23] a precursor of Ti_3SiC_2 (TSC, one of typical MAX materials, Figure S1a−c) powders with a dimension of ~ 3 μm has been prepared by a high-pressure sintering method. Subsequently, some particles
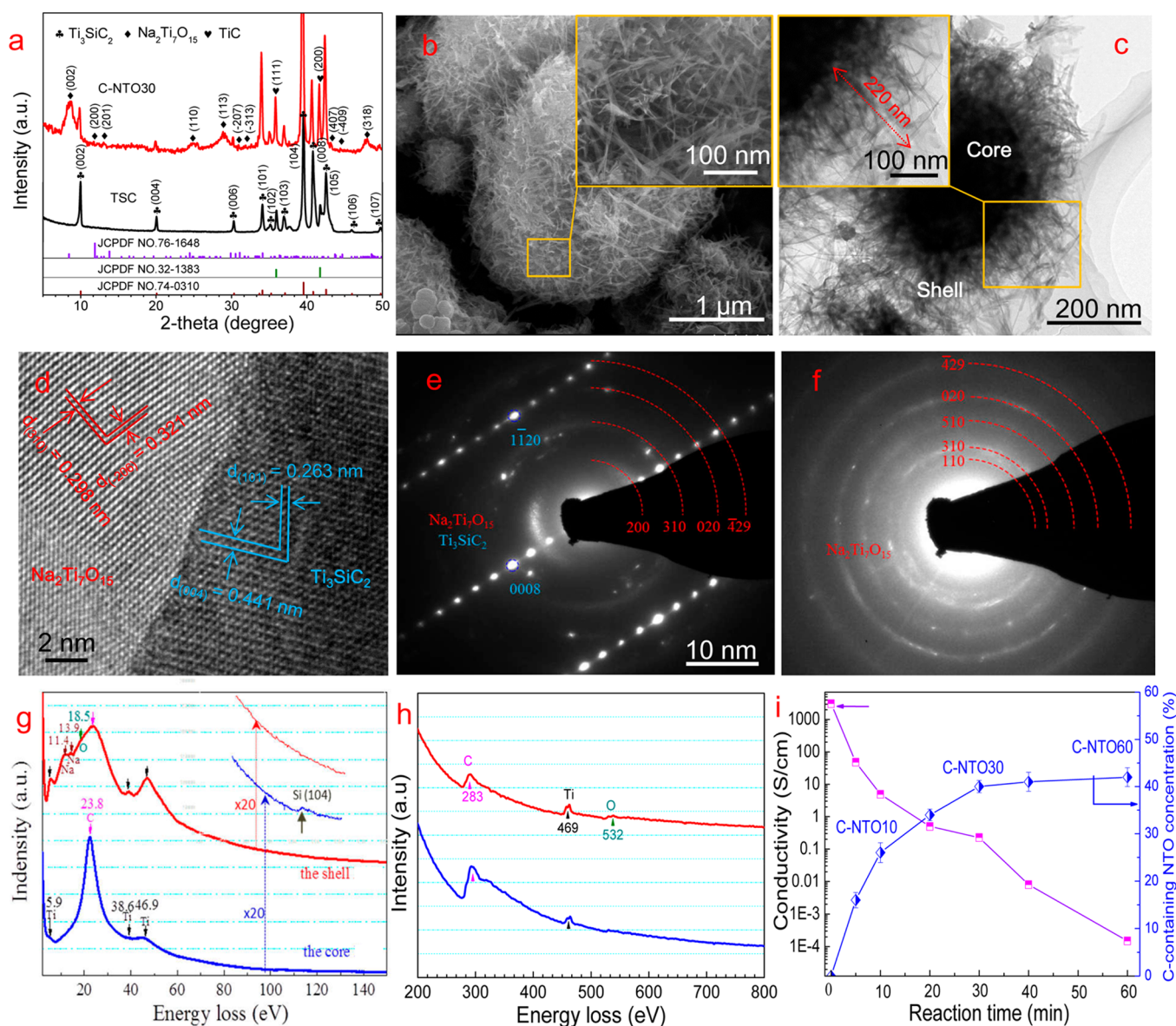
Figure 2. Microstructure characterizations. (a) XRD patterns of typical TSC and C-NTO30 samples. (b) Representative FESEM image of the C-NTO30 composite. The inset is a high magnification of the SEM image. (c) Typical TEM image of a core−shell C-NTO30 sample. The inset is a high magnification of the TEM image. (d) HRTEM image of the interface (C-NTO30). (e) SAED pattern of the core (TSC). (f) SAED pattern of the shell (C-containing $Na_2Ti_7O_{15}$). (g, h) Low-loss and core-loss EELS of the core and shell, respectively. (i) Effect of microwave reaction time on the conductivity and the concentration of C-containing NTO.

with urchin-like morphology are observed (Figure S1d) with the help of the microwave reaction between the precursor and NaOH solutions (the detailed procedure is described in the Methods section) followed by annealing under the protection of pure Ar gas at 450 °C for 2 h. The X-ray diffraction (XRD) patterns of the as-sintered samples (Figure 2a) are mostly indexed to be the TSC phase (JCPDF No. 74-0310), with some minor TiC peaks (∼2 wt %, JCPDF No. 32-1383) that are formed during the sintering process.[17] Taking into account the low concentration and the weak chemical reaction activity of TiC, the effect of TiC on the electrochemical performance is neglected throughout the following discussion.[19] As a result, the precursor after the microwave reaction in NaOH solutions followed by annealing is mainly composed of Ti_3SiC_2 and $Na_2Ti_7O_{15}$ (denoted as NTO, JCPDF No. 76-1648) phases. The concentration of the NTO phase is ∼40 wt % based on

both the inductively coupled plasma (ICP) and the energy dispersive X-ray spectrometry (EDX) analysis results (Tables S1 and S2), similar to that of samples fabricated by the hydrothermal reaction method.[19]

The morphology of the urchin-like products has been investigated in detail by field-emission scanning electron microscopy (FESEM) and transmission electron microscopy (TEM). Urchin-like particles covered with nanoscale fibers are observed (Figure 2b). Additionally, the cross-linked nanofibers form a large number of micro/mesopores (Figure 2c), which can be further confirmed by the nitrogen adsorption− desorption measurement. The TEM image (Figure 2c) reveals a great number of nanofiber arrays on the surface of the TSC, forming a typical core−shell heterogeneous composite. The dimension of the TSC cores is 300 ± 50 nm. The length and width of the exterior layer nanofibers (NTO) are ∼220 and
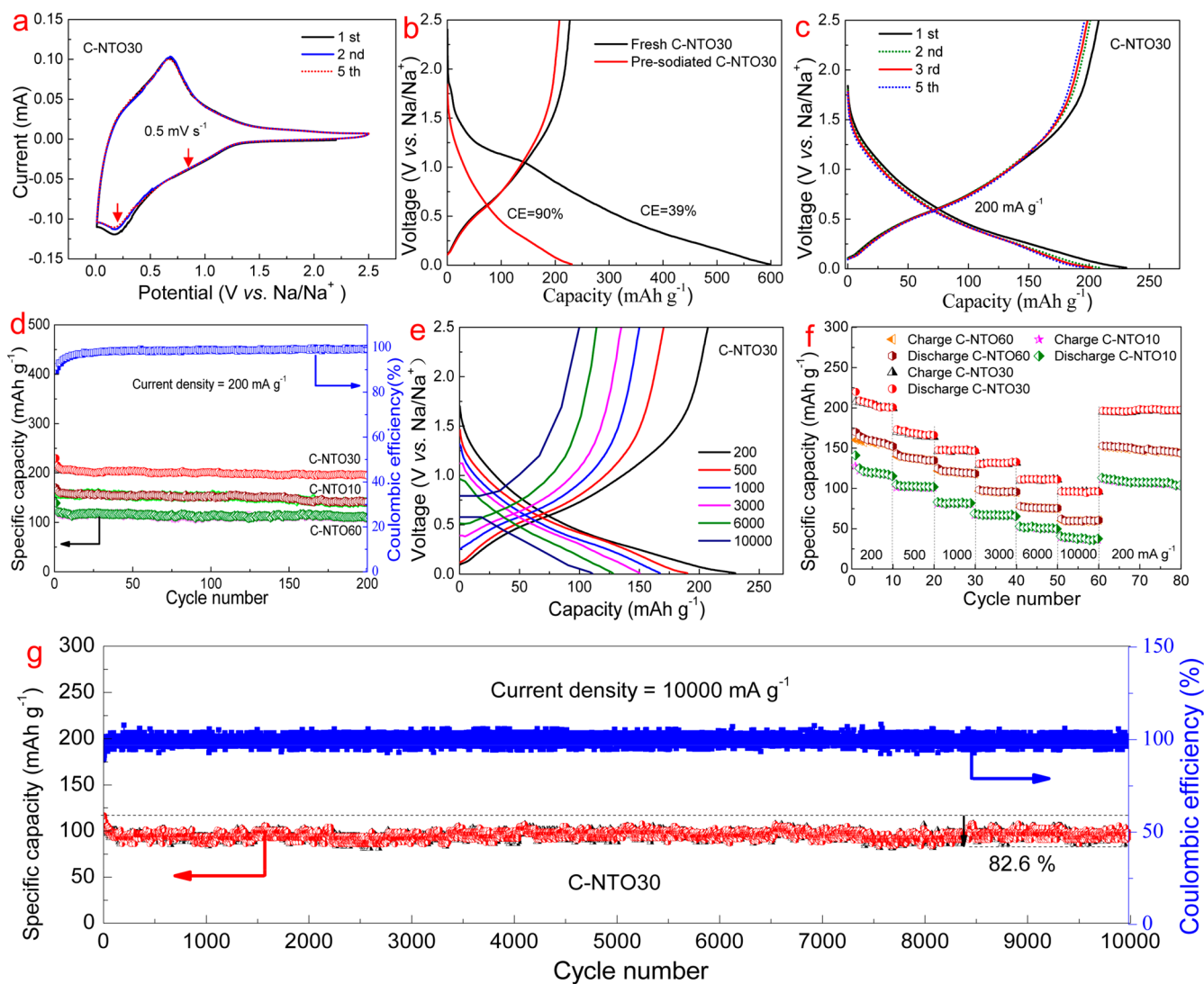
Figure 3. Na storage properties at 25 °C. (a) Cyclic voltammograms of the C-NTO30 recorded at a scan rate of 0.5 mV s^{-1} over a voltage range of 0.01−2.5 V *versus* Na/Na$^+$. (b) Initial galvanostatic curves of the fresh and presodiated C-NTO30 electrodes. (c) Initial discharge−charge curves of the C-NTO30 sample. (d) Long-term cycling performance of the three C-NTO samples at 200 mA g^{-1}. Coulombic efficiency is plotted for the C-NTO30 sample only. (e) First discharge−charge profiles of the C-NTO30 sample at a current range of 200−10000 mA g^{-1}. (f) Rate performance of the three samples at a current range of 200−10000 mA g^{-1}. (g) Cycling property of the C-NTO30 electrode at a current rate of 10 000 mA g^{-1}. Coulombic efficiency remains 82.6% after 10 000 cycles.

~10 nm, respectively. The high-resolution transmission electron microscopy (HRTEM) image (Figure 2d) exhibits an interface between NTO and TSC. The selected area electron diffraction (SAED) pattern shows the core is composed of both NTO and TSC (Figure 2e), and the shell consists of NTO (Figure 2f), suggesting the formation of a core−shell structure. In addition, low-loss and core-loss of electron energy loss spectroscopy (EELS) in Figure 2g,h show that the core is mainly composed of Ti (5.9, 38.6, 46.9, and 469 eV), Si (104 eV), and C (23.8 and 283 eV), which is consistent with the SAED pattern. In contrast, the Si peak is eliminated in the shell, and it contains a C peak besides Na, Ti, and O (532 eV). It demonstrates that the Si layer is removed. Although the C-containing concentration and the sites where C atoms hold remain unclear owing to the interference of the C-containing matrix, the occurrence of C-containing concentration in the NTO compound is confirmed. This reaction is also evidenced by the improved conductivity of the NTO compound, as shown in the following section. The thermal gravimetric analysis and

XRD pattern suggest that this composite shows high thermal stability (Figure S2a). Although it is prone to adsorb water molecules at low temperatures (below 150 °C), the main phase composition remains invariable. When the temperature is higher than 350 °C, the TSC core is continuously oxidized.[24]

To interpret the formation process of the core−shell MAX@ C-NTO, the morphology evolution is monitored at different NaOH concentrations and reaction times. Below 0.1 M almost no NTO phase is formed due to the slow reaction kinetics (Figure S3). The most suitable NaOH concentration to form the core−shell structure is ~2.0 M, above which (~5.0 M) will result in the rapid coarsening of the NTO (Figure S4a−d) or even the elimination of the core−shell heterogeneous structure (Figure S5a). Besides, as the reaction proceeds, the surface of the TSC first becomes rough, with the formation of irregular fibers (Figure S4e−h), indicating the transformation of the TSC surface into the NTO. With increasing incubation time, the size of the TSC core decreases and an urchin-like morphology is achieved (~30 min). Note that some coarsened
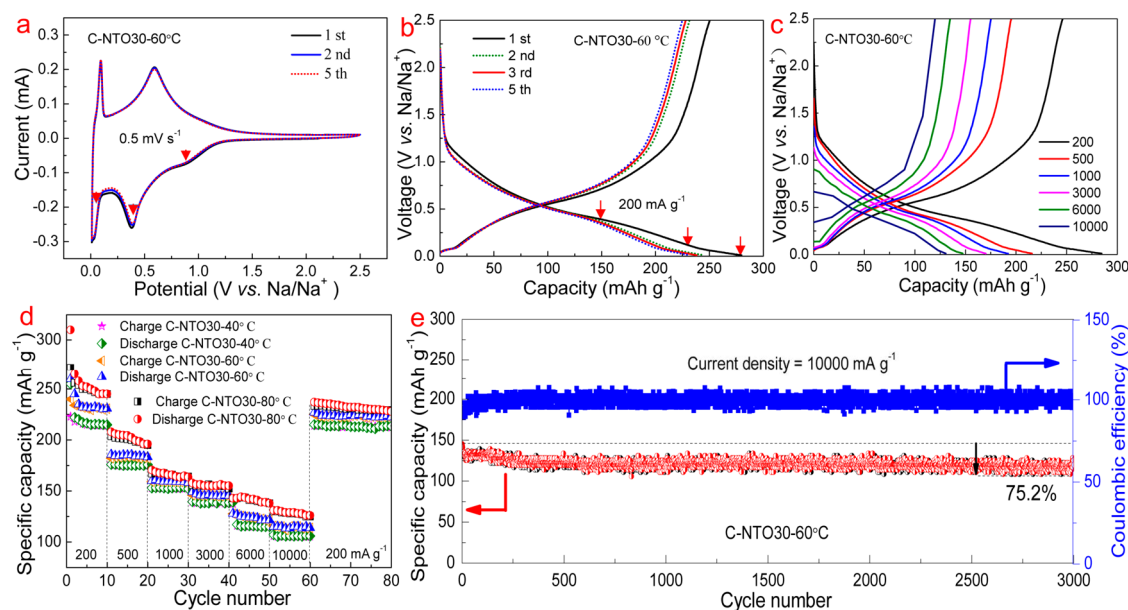
Figure 4. Na storage properties of the C-NTO30 sample at elevated temperatures. (a) Cyclic voltammograms of the C-NTO30-60 °C sample recorded at a scan rate of 0.5 mV s^{-1} over a voltage range of 0.01−2.5 V vs Na/Na$^+$. (b) Initial charge−discharge profiles of the C-NTO30-60 °C sample with a current density of 200 mA g^{-1}. (c) First discharge−charge profiles of the C-NTO30-60 °C sample at a current range of 200−10 000 mA g^{-1}. (d) Rate performances of the different samples at a current range of 200−10 000 mA g^{-1}. (e) Cycling property of the C-NTO30-60 °C electrode at a current rate of 10 000 mA g^{-1}. Coulombic efficiency remains 75.2% after 3000 cycles.

NTO bars are observed with further increasing the reaction time.

The TSC has a high conductivity but low Li and Na storage capacity.[19,25] On the contrary, the NTO has a high capacity, yet its conductivity is low.[26−30] Therefore, the NaOH concentration and the reaction time are very important to control the formation of the core−shell structure with an optimal capacity and conductivity by tailoring the phase fraction of the TSC and the NTO phases. The effect of reaction time on both the NTO concentration and the conductivity of the composites has been investigated (Figure 2i). At the initial reaction process, the NTO concentration is increased with an increasing incubation time, and it changes from ∼25 wt % (10 min) to ∼40 wt % (30 min). By further increasing the incubation time, the concentration of the NTO phase only slightly increases, and then it remains at a constant value around 44 wt %. In comparison, the effect of the incubation time on the conductivity is complex. Specifically, the conductivity of the pristine TSC powder ($t = 0$) is ∼0.9 × 10^3 S/cm, slightly lower than that of the previously reported value of the bulk material.[17] With increasing the reaction time to 30 min, the conductivity decreases, down to ∼0.2 S/cm. A sharp reduction in the conductivity is observed with a further increase in the incubation time, probably due to the aggregation and coarsening of the NTO (Figure S4h). It is interesting to note that the sample after reacting with 5.0 M NaOH solutions for 30 min shows the highest NTO concentration of ∼91 wt % (Figure S6a), with the conductivity being ∼3.5 × 10^{-3} S/cm. It demonstrates that the fraction of the NTO phase in the heterogeneous composite is critical to tailoring the conductivity. Compared with the conductivity of the pure NTO (10^{-4}−10^{-6} S/cm), the value of the 91 wt % NTO is significantly improved, implying that it is partially attributed to the C-containing concentration induced during the reaction process. In consideration of the amount of C-containing NTO and the conductivity of the composite, a reaction time of 30

min is desirable, in which a core−shell MAX@C-NTO with a ∼40 wt % C-containing NTO and high conductivity is achieved. This trend is similar to the hydrothermal-prepared MAX@K$_2$Ti$_8$O$_{17}$ composite that we reported previously.[19]

Na Storage Properties at 25 °C. The electrochemical performances of these heterogeneous C-NTO composites have been evaluated to assess their potential as alternative anode materials for SIBs. Three samples fabricated in 2 M NaOH solutions at 200 °C at different times (denoted as C-NTO10, C-NTO30, and C-NTO60, where the Arabic numbers in the notation represent the reaction time) are employed to investigate the effect of the NTO concentration and the conductivity on Na storage. The three composites show similar morphologies but different phase fractions (Figure 2a,b and Figures S5 and S6b). The typical cyclic voltammetry (CV) curves of the C-NTO30 show a couple of obvious redox peaks at 0.25/0.69 V in the initial cycles (Figure 3a), which are related to the Na-ion insertion/extraction processes.[31] Comparatively, a pair of weak redox peaks at 1.12/1.25 V can be assigned to the reversible reaction of Ti^{3+}/Ti^{4+}.[31] Irrespective of the carbon contents, the C-NTO30 electrode exhibits a large capacity on the first discharge process, approaching 600 mAh g^{-1} (Figure 3b). However, the initial charge capacity is only ∼227 mAh g^{-1}, corresponding to a Coulombic efficiency (CE) of 39%, which is also suggested by the large void between the first cycle and the second cycle in the initial CV curves (Figure S7). Attractively, the CE can be improved from 39% to 90% after a simple presodiation process by contacting the electrode and the Na metal filled in the electrolyte for 5 min (Figure 3b). Therefore, all the following tests have been performed after treatment.

Previous testing results confirm that the capacity contribution from the TSC compound (∼10 mAh g^{-1}) can be neglected, and it merely acts as a charge collection and interlinking transport path. The representative charge−discharge curves of the three C-NTO samples in the first few cycles at a current density of 200 mA g^{-1} between 2.50 and 0.01
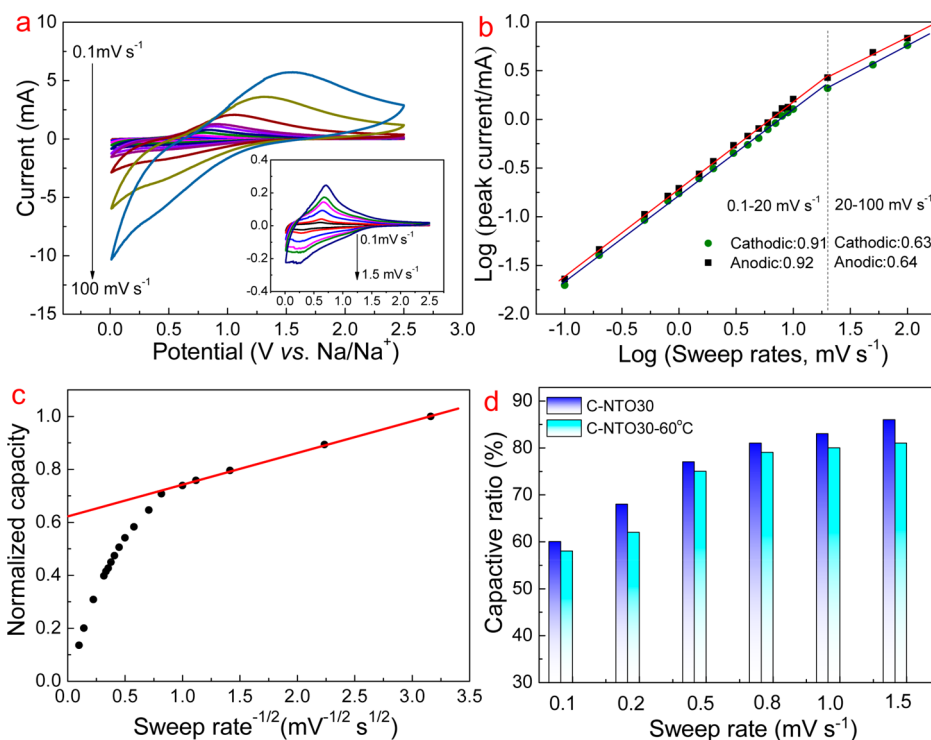
Figure 5. Pseudocapacitance of the C-NTO30 electrode. (a) Room-temperature cyclic voltammetry curves at sweep rates from 0.1 to 100 mV s^{-1}. (b) b-Value determined by the relationship between the peak currents and the sweep rates. (c) Normalized capacity *versus* sweep rate$^{-1/2}$. (d) Capacitive ratios of the C-NTO30 and C-NTO30-60 °C electrodes at different sweep rates.

V (Figure 3c and Figure S8a,b) reveal a reversible intercalation reaction.[12,15] These Ti-based compounds usually exhibit several plateaus during the Li/Na ion intercalation–extraction process.[19] The rapid capacity decay in the first cycles can be generally attributed to the accompanying decomposition of electrolyte and the formation of a solid–electrolyte interfacial (SEI) film.[9,18]

The C-NTO30 sample delivers an initial discharge capacity of 230 mAh g^{-1}, much higher than ~170 and ~140 mAh g^{-1} for the C-NTO10 and the C-NTO60 samples, respectively. During the subsequent cycling, the discharge capacity of the C-NTO30 sample remains stable, and it only reduces to ~200 mAh g^{-1} after 200 cycles. Similar trends are detected for the C-NTO10 and C-NTO60 samples with capacities of ~150 and ~125 mAh g^{-1} at the 200th cycle, respectively (Figure 3d). Notably, the energy storage capacity of the nanostructured anodes adopted intercalation reaction mechanisms with large surface area which often exceeded their theoretical value (Na$_2$Ti$_7$O$_{15}$, ~64 mAh g^{-1}).[32] This is due to (i) the reversible decomposition of the electrolyte associated with the formation of an SEI layer and (ii) the extra Na$^+$ adsorption–desorption on the SEI corresponding to interfacial storage.[33]

The rate capability plays a crucial role in developing Na storage materials. The first discharge–charge curves of the three samples under different current rates from 200 to 10 000 mA g^{-1} have been investigated (Figure 3e and Figure S8c,d). The C-NTO30 sample delivers reversible capacities of 230, 189, 165, 149, and 128 mAh g^{-1} at current rates of 200, 500, 1000, 3000, and 6000 mA g^{-1}, respectively. Notably, a high capacity of more than 110 mAh g^{-1} is delivered even at an extremely high current density of 10 000 mA g^{-1}. For the C-NTO10 and the C-NTO60 samples, the corresponding capacities at the same current rate are lower than that of the

C-NTO30. To further probe the extraordinary rate capability, three electrodes are cycled 10 times at each current rate (Figure 3f). All of them show similar trends. Regardless of the rapid change in current density, the capacity level remains stable at each rate. Specifically, the values at high current rates are more stable than those at low current rates. Moreover, a reversible capacity of ~93 mAh g^{-1} at 10 000 mA g^{-1} is retained without any appreciable capacity decay (82.6% capacity retention) even after more than 10 000 cycles (Figure 3g), higher than those of the C-NTO10 and C-NTO60 counterparts (Figure S9) and almost all other high-performance Ti-based materials at high rates reported so far (Table S3).

Na Storage Properties at Elevated Temperatures. To extend the SIB applications and test their safety, Na storage properties of the C-NTO30 electrode at 40, 60, and 80 °C (denoted as C-NTO30-40 °C, C-NTO30-60 °C, C-NTO30-80 °C) have been investigated (Figures 4 and Figures S10 and S11). The similar electrochemical behaviors are detected in the temperature range of 40–80 °C. Basically, the initial capacity is increased and the cycle stability is reduced with increasing the temperature due to the increased diffusivity of Na ions and electrolyte activity. For example, the initial specific capacity of the C-NTO30 at 60 °C increases to ~1.28 times as high as that of the battery operated at 25 °C (Figure 4b). By increasing the cycle number, the capacity contributed by 0.02/0.08 V in the redox pair was sharply reduced (Figure 4a). Thus, this pair might be related to the reaction between the active material and the electrolyte, although the corresponding chemical reaction is uncertain due to the complication of SEI. Additionally, analogous to the batteries tested at 25 °C, the discharge capacity at the first cycle with a current density of 200 mA g^{-1} slightly increases to ~255 mAh g^{-1} (40 °C), ~280 mAh g^{-1} (60 °C), and ~330 mAh g^{-1} (80 °C), and then the stable values of
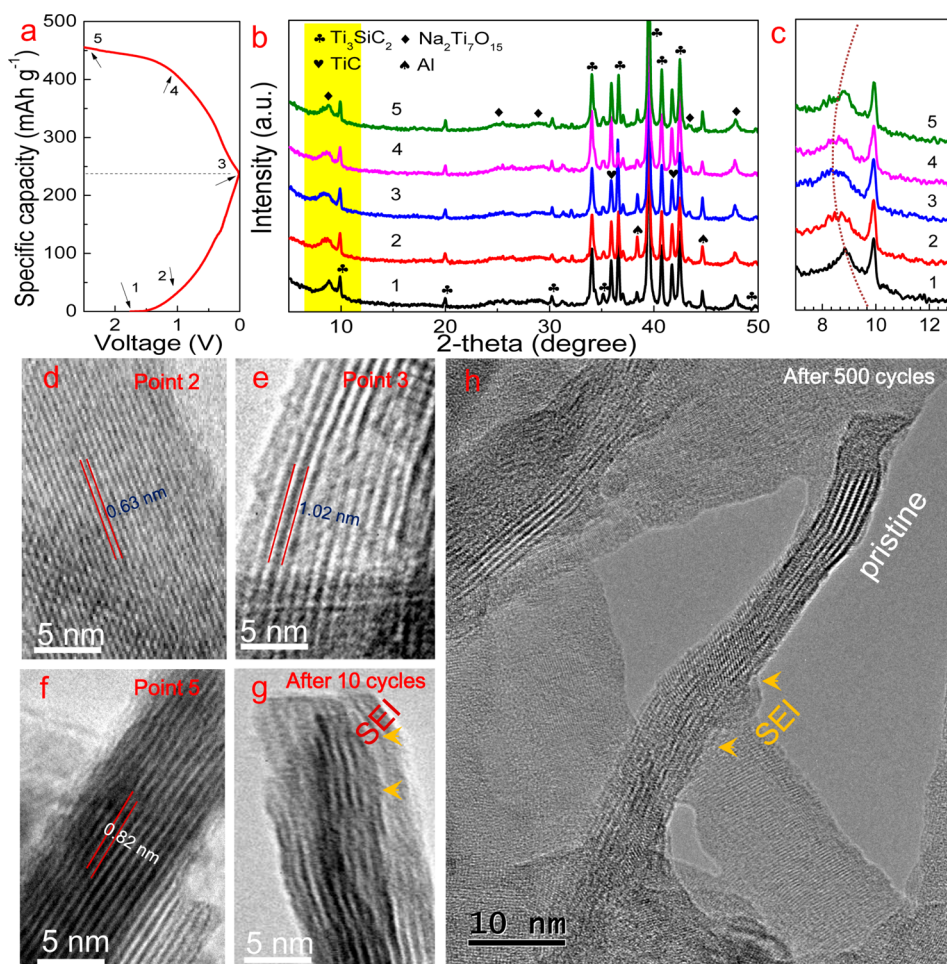
Figure 6. *Ex situ* microstructural variation of the C-NTO30 electrode during the charge−discharge procesing. (a) Typical charge−discharge curves of the C-NTO30 electrode; (b) XRD patterns of the C-NTO30 electrode at different stages; (c) high-magnification patterns in yellow area in (b). (d−g) HRTEM images of the C-NTO30 electrode at selected charged/discharged states at 25 °C (current density = 200 mAg⁻¹). (h) HRTEM of the C-NTO30 electrode materials after 5000 cycles.

~206 mAh g⁻¹ (40 °C), ~225 mAh g⁻¹ (60 °C), and ~238 mAh g⁻¹ (80 °C) are maintained after 200 cycles (Figure 4b and Figure S10).

Owing to the easy decomposition of the electrolyte and the instability of the SEI, the rate performance at high temperatures becomes one of the most critical issues in the field of battery applications. Principally, the C-NTO30 sample exhibits similar trends at both 25 and 60 °C. Compared with those under different rates at 25 °C, the first specific discharge capacity of the C-NTO30 sample at 60 °C (C-NTO30-60 °C) is enhanced correspondingly. Moreover, the cell that is cycled 10 times at each current rate also retains a stable capacity at each rate. Finally, a specific capacity of 222 mAh g⁻¹ has been attained when the current density returns back to the initial value of 200 mA g⁻¹ after 60 cycles, indicating this material has a high electrochemical reversibility (Figure 4d). Accidentally, for the C-NTO30 sample, a reversible capacity of ~120 mA h g⁻¹ at 10 000 mA g⁻¹ is retained without any appreciable capacity decay even after more than 3000 cycles at 60 °C. The high capacity retentions are achieved at elevated temperatures (Figure 4e and Figure S11), wherein the values are 81.5% (10 000 cycles, at 40 °C), 75.2% (3000 cycles, at 60 °C), and 59.5% (1000 cycles, at 80 °C), respectively. To the best of our knowledge, a combination of ultrahigh rate performance and ultralong cycle lifetime with good capacity retention at elevated

temperatures has been achieved, and an average fading percentage per cycle outperforms those of anode materials for both LIBs and SIBs at high temperatures (Table S4).

Kinetics of Na Intercalation. Compared with pure NTO or NTO-based composites, both the capacity and rate performance of the presodiated C-NTO samples have been significantly improved. To interpret the superior capacity and outstanding rate performance, the pseudocapacitances of the heterogeneous C-NTO30 sample at 25 and 60 °C have been analyzed by CV techniques.[34,35] The C-NTO30 sample (Figure 5a) at 25 °C displays similar CV curves with broad peaks during both cathodic and anodic processes at various sweep rates ranging from 0.1 to 100 mV s⁻¹. According to the relationship between the measured peak current (i) and the scan rate (v) displayed in eq 1:[12,35,36]

$$i = av^b \tag{1}$$

where a is a constant and b can be determined by the slope of the $\log(v)−\log(i)$ plots. A b-value of 0.5 represents that the current is controlled by semi-infinite linear diffusion; a value of 1 indicates that the current is a surface-capacitive-controlled process.

As shown in Figure 5b, high b values of 0.91 (cathodic peaks) and 0.92 (anodic peaks) are observed in the scan rate range of 0.1−20 mV s⁻¹, suggesting that the kinetics of the C-NTO30
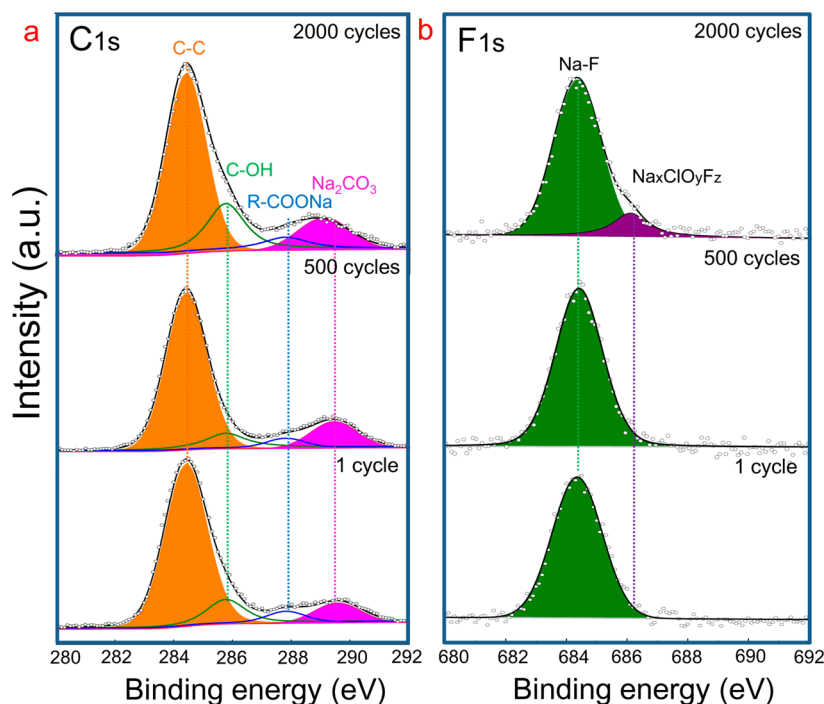
Figure 7. *Ex situ* XPS profiles of the C-NTO30 samples after different cycles at 25 °C. (a) C 1s spectrum. Both C−OH and Na$_2$CO$_3$ peaks remain stable with increasing cycle number. (b) F 1s spectrum. A Na$_x$ClO$_y$F$_z$ peak is detected after 2000 cycles.

electrode exhibits capacitive characteristics. The *b* values quantified at scan rates above 20 mV s^{-1} decrease to 0.63 (cathodic peaks) and 0.64 (anodic peaks), respectively.

Similar phenomena are also observed in T-Nb$_2$O$_5$ oxide electrodes.[37] The rate capability of the C-NTO30 is mainly determined by an increase in the ohmic contribution and/or diffusion constraint upon a fast scan rate. Based on the classical Trasatt's method,[34] the plot of capacity *versus* $v^{-1/2}$ demonstrates that the capacity does not vary significantly as the scan rate increases within the range of 0.1−1.5 mV s^{-1} (Figure 5c). Thus, the total capacitive contribution at a certain scan rate is calculated by separating the specific capacity contribution from the capacitive and diffusion-controlled charges at a fixed voltage.[35] As shown in Figure 5d, quantitative calculation results show that the capacitive ratio is gradually improved by increasing the scan rate, reaching a maximum value of 83.1% at 1.5 mV s^{-1}. By comparison, a similar trend is detected for the C-NTO30 sample at 60 °C. The existence of high Na intercalation pseudocapacitance (the max value of 78.9%, Figure 5d and Figure S12) accounts for the ultrahigh rate performance.

In addition, the relationship between kinetics and the electrochemical performance is also measured by electrochemical impedance spectroscopy (EIS). Nyquist plots (Figure S13) of the different C-NTO electrodes after activation in frequencies over the range of 100 kHz to 0.1 Hz show the same feature of a depressed semicircle at high frequency (charge-transfer resistance, R_{ct}), and a linear part at low frequency (Warburg impedance, Z_w). The smallest R_{ct} for the C-NTO10 (Table S5) confirms that the high rate performance is related to the core−shell heterogeneous structure, in which the residue TSC provides a convenient channel for electron transfer. With increasing the temperature, both the R_{ct} and Z_w are reduced, indicating the electrons and ions can readily penetrate through the SEI layer.[14]

Mechanism of Na Storage. From the shape of the charge−discharge curves and the large irreversible capacity in the initial cycle, we infer that the electrochemical reaction of MAX@C-NTO belongs to the intercalation reaction mechanisms. To follow the structural changes during sodiation and desodiation, *ex situ* XRD measurement as a function of the state-of-charge/discharge has been carried out (Figure 6a−c, wherein points 1−3 are assigned to the intercalation process and points 4 and 5 are assigned to the extraction process). There are no additional peaks associated with other types of structures that can be observed during cycling, indicating that no other phase is formed during cycling.[38] Specifically, on discharge (sodiation), the original C-NTO30 heterogeneous structure is maintained up to the cutoff voltage of 0.01 V. Indeed, the HRTEM results (Figure 6d) show that there is a slight change in the lattice spacing after the sodiated process (∼0.72 nm, at point 2) compared to the pristine C-NTO30 (∼0.63 nm). Comparatively, at point 3 (0.01 V), the XRD peaks corresponding to the NTO become slightly broadened (Figure 6c) and the lattice spacing changes to 1.02 nm (Figure 6e), releasing a reversible capacity of ∼225 mAh g^{-1}. This process mainly relates to the insertion of a large Na ion into the NTO host. After desodiation, the XRD peaks of the NTO shift toward the large angle direction, indicating the contraction of lattice spacing,[39] which can be further confirmed by the HRTEM (Figure 6f, ∼0.82 nm). In addition, the surface of the electrode materials is covered by a separated SEI film after 10 cycles (Figure 6g). Note that both the thin SEI film and the structure of the NTO remain well even after 5000 cycles (Figure 6h). Similar results are also confirmed for the C-NTO30 at 60 °C (Figure S14). It is believed that the stable long-term cycling performance of C-NTO30 is associated with the formation of a thin and uniform SEI film. The good elevated properties are related to the prohibition of particle aggregation (Figure S15).

To analyze the composition changes of the SEI layer, *ex situ* X-ray photoelectron spectroscopy (XPS) measurements have been performed for the C-NTO30 and C-NTO30-60 °C samples at different cycles (Figure 7 and Figure S16). The C 1s and the F 1s spectra at different cycles are compared. The C−C peak in Figure 7a is assigned to the TSC, and the C−OH peak is related to the adhered additive. The Na_2CO_3 peak is detected even after 1 cycle (Figure 7a), revealing the formation of an SEI layer *via* electrolyte (fluoroethylene carbonate, FEC) decomposition illustrated by eq 2:[14,40]

$$FEC + Na^+ + e^- \rightarrow CH_2 = CHF + Na_2CO_3 \qquad (2)$$
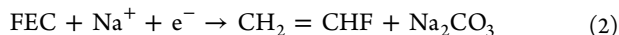
Analogous to that of LIBs, the volume variation during the Na^+ insertion and extraction processes hinders the SEI structure integrity, and thus the formed Na_2CO_3 seems to be located underneath the SEI layer. In contrast, a high $Na_xClO_yF_z$ (Figure 7b) peak after 2000 cycles suggests that the decomposition of FEC occurs. Thus, the similar morphology and intensity of the Na_2CO_3 peak show the SEI film is very stable, and the reduced capacity might be related to the decomposition products from $NaClO_4$ during the cycling process.[41] Similar peak variations are found for the C-NTO30-60 °C electrode, due to the same reaction mechanism. Comparatively, the increased $Na_xClO_yF_z$ peak intensity indicates that a more serious decomposition of FEC occurred during the cycling process at elevated temperature.

Finally, the capacity and rate performance are also affected by the specific surface area and pore-size distribution of the heterogeneous materials. Compared with pristine TSC and other C-NTO samples, the C-NTO30 sample has the largest BET surface areas of ~49.5 m^2 g^{-1} (Figure S17), which could bestow more adsorbtion sites for Na^+ storage. In turn, although a high concentration of the NTO can be attained in C-NTO60, the elimination of 1.8−1.9 nm pores reduces not only the volume-adsorbed value but also the capacity. Therefore, the enhanced capacity and kinetics of the C-NTO30 in a wide temperature range are related to high pseudocapacitance, a stable and thin SEI film, and large micro/mesopore structure.

CONCLUSION

In summary, a heterogeneous Ti_3SiC_2@ C-containing $Na_2Ti_7O_{15}$ (MAX@C-NTO) composite prepared by microwave-assisted alkaline treatment of a MAX (Ti_3SiC_2) precursor has been reported. The electrical conductivity and the concentration of the C-containing $Na_2Ti_7O_{15}$ for MAX@C-NTO can be rationally tailored by controlling the NaOH concentration and the reaction time. The synthesized MAX@C-NTO composites show excellent sodium storage performances in a wide temperature range (25−80 °C) in terms of high reversible capacity, long cycle stability, and high rate capability. A capacity of ~93 mA h g^{-1} is retained without apparent capacity fading at 25 °C, even after more than 10 000 cycles at a high rate of 10 000 mA g^{-1}. More attractively, a high capacity retention is attained at an ultrahigh rate of 10 000 mA g^{-1} at elevated temperatures. This heterogeneous architecture has shown several advantages in SIBs including the uniform distribution of conductive materials, the facilitation of electron and sodium ion transportation in interlinked nanofibers, and the depression of active material aggregation. This MAX@C-NTO composite with innovative compositional and structural advantages provides an effective strategy to synthesize other

sodium/lithium-hosting materials with large capacity and temperature tolerance.

METHODS

Microwave-Assisted Synthesis of Ti_3SiC_2@C-NTO. All analytical-grade chemicals and raw materials were used as received. In a typical experiment, Ti_3SiC_2 was synthesized by a high-pressure sintering method (1 GPa, 1500−1700 °C) using commercial Ti (99.5% purity, 325 mesh, Aladdin Reagent), Si (99.9% purity, 40−200 mesh, Aladdin Reagent), and C (99.5% purity, 2−4 μm, Aladdin Reagent) as starting materials, which was similar to that reported in our previous work.[19,23,42] Then, Ti_3SiC_2(1.0 g) was added into 50 mL of a 0.1−5 M NaOH aqueous solution. After vigorous stirring for 30 min, the resultant dispersion was then transferred to a 100 mL Teflon-lined high-strength shell (polyether ether ketone) autoclave. A microwave system (MS, XH-8000, Beijing XiangHu Science and Technology Development Co., Ltd., China) equipped with *in situ* magnetic stirring was used to heat the autoclave. The mixture was heated to 120 °C within 8 min with a power of 500 W and subsequently to 160 °C at a heating rate of 10 °C/min. Then, the temperature was increased to 200 °C using a ramp rate of 8 °C/min and kept for 5−60 min with a power of 600 W. After the microwave reaction, the reaction product was centrifuged at 3500 rpm three times using DI water and absolute ethyl alcohol. The suspension was freeze-dried under vacuum overnight on a freeze-dryer (FD-1A-80, Beijing Boyikang Laboratory Instrument Co. Ltd.). Then, the targeted C-NTO powsers were obtained by annealing the freeze-dried samples under the protection of pure Ar gas at 450 °C for 2 h.

Material Characterization. XRD patterns were collected on a Rigaku D/Max-2500 diffractometer using a filtered Cu Kα radiation at a sweep rate of 2°/min from 5 to 50°. The accelerating voltage and current were 40 kV and 200 mA, respectively. *Ex situ* XRD samples of the charge−discharge C-NTO anodes were rinsed with propylene carbonate solution and dried under vacuum at room temperature for 12 h. To obtain the morphologies and elemental compositions of C-NTO, a scanning electron microscopy (SEM) was conducted with a Hitachi S-4800 equipped with an energy dispersive X-ray detector spectrometer (Horiba, EMAX). According to our previous method,[19] the concentrations of $Na_2Ti_7O_{15}$, TiC, and Ti_3SiC_2 were determined. TEM images and EELS analysis were observed on a Titan ETEM G2 at 300 kV. ICP (ICAP 6300 Thermo Scientific) was used to analyze the concentrations of the elements (Ti, Si, K) of the obtained samples. A H7756 four-point probe was used to determine the electrical conductivity of the obtained samples. Thermogravimetric analysis (TGA) was conducted on a thermal analysis instrument (Netzsch STA449C, Germany) in air at a heating rate of 10 °C/min. The surface areas and pore size distribution of the samples were performed on a Micrometrics ASAP2020 analyzer at −196 °C (77 K). XPS was conducted on a ThermoFisher X-ray photoelectron spectrometer with Al Kα (1486.71 eV) X-ray radiation (15 kV and 10 mA). The binding energies obtained in the XPS analysis were corrected by referencing the C 1s peak position (284.40 eV) and the F 1s peak position (684.51 eV).[14]

Electrochemistry Testing. The working electrodes were prepared by dispersing the 80 wt % active materials (C-NTO), 10 wt % acetylene carbon black, and 10 wt % sodium alginate (NaAlg) in an appropriate amount of distilled water. The resultant slurry was coated on the aluminum foil substrate using an automatic film applicator and dried under vacuum at 110 °C for 12 h. To obtain electrodes of a well-connected structure and high tap density, the prepared electrodes were rolled on a rolling machine (MSK-2150, Shenzhen Kejing Materials Technology Co., LTD, China). Coin-type cells (CR 2032) were assembled in a high-purity argon-filled glovebox with the moisture and oxygen level below 0.1 ppm and tested at 25, 40, 60, and 80 °C, respectively. The temperature was controlled by a programmable box (GDJS-100, Beijing YaShiLin Testing Equipment Co., Ltd., China). Sodium foil was used as the counter and reference electrodes. The electrolyte was made of 1.0 M $NaClO_4$ in an ethylene carbonate and

propylene carbonate solution at 1:1 volume ratio, with 5 wt % addition of FEC. The separator was a glass fiber filter (GF/D, Whatman).

Galvanostatic charge–discharge tests were performed over a voltage range of 0.01–2.5 V (vs Na$^+$/Na) using a battery measurement system (Land CT2001A). CV measurements were conducted on a Biologic VMP3 electrochemical workstation at a sweep rate of 0.1–100 mV s^{-1} at 25 and 60 °C, respectively. EIS characterization was carried out on a BioLogic VMP3 system with the typical frequency range from 100 kHz to 0.1 Hz by applying the applied ac voltage of 5 mV at 25 and 60 °C, respectively.

ASSOCIATED CONTENT

Ⓢ Supporting Information

The Supporting Information is available free of charge on the ACS Publications website at DOI: 10.1021/acsnano.7b05559.

Additional figures and tables as described in the text (PDF)

AUTHOR INFORMATION

Corresponding Author

*E-mail: pengqiuming@gmail.com.

ORCID Ⓓ

Qingrui Zhang: 0000-0002-2070-2179
Qiuming Peng: 0000-0002-3053-7066

Notes

The authors declare no competing financial interest.

ACKNOWLEDGMENTS

REFERENCES

(1) Dunn, B.; Kamath, H.; Tarascon, J. M. Electrical Energy Storage for the Grid: A Battery of Choices. *Science* **2011**, *334*, 928−935.

(2) Xiang, X.; Zhang, K.; Chen, J. Recent Advances and Prospects of Cathode Materials for Sodium-Ion Batteries. *Adv. Mater.* **2015**, *27*, 5343−5364.

(3) Hou, H.; Banks, C. E.; Jing, M.; Zhang, Y.; Ji, X. Sodium-Ion Batteries: Carbon Quantum Dots and Their Derivative 3D Porous Carbon Frameworks for Sodium-Ion Batteries with Ultralong Cycle Life. *Adv. Mater.* **2015**, *27*, 7895−7895.

(4) Simon, P.; Gogotsi, Y.; Dunn, B. Where Do Batteries End and Supercapacitors Begin? *Science* **2014**, *343*, 1210−1211.

(5) Wu, C.; Jiang, Y.; Kopold, P.; Van Aken, P. A.; Maier, J.; Yu, Y. Peapod-Like Carbon-Encapsulated Cobalt Chalcogenide Nanowires as Cycle-Stable and High-Rate Materials for Sodium-Ion Anodes. *Adv. Mater.* **2016**, *28*, 7276−7283.

(6) Doeff, M. M.; Ma, Y.; Visco, S. J.; De Jonghe, L. C. Electrochemical Insertion of Sodium into Carbon. *J. Electrochem. Soc.* **1993**, *140*, L169−L170.

(7) Park, M.-H.; Kim, M. G.; Joo, J.; Kim, K.; Kim, J.; Ahn, S.; Cui, Y.; Cho, J. Silicon Nanotube Battery Anodes. *Nano Lett.* **2009**, *9*, 3844−3847.

(8) Wang, S.; Wang, L.; Zhu, Z.; Hu, Z.; Zhao, Q.; Chen, J. All Organic Sodium-Ion Batteries with Na$_4$C$_8$H$_2$O$_6$. *Angew. Chem.* **2014**, *126*, 6002−6006.

(9) Abel, P. R.; Fields, M. G.; Heller, A.; Mullins, C. B. Tin-Germanium Alloys as Anode Materials for Sodium-Ion Batteries. *ACS Appl. Mater. Interfaces* **2014**, *6*, 15860−15867.

(10) Sottmann, J.; Herrmann, M.; Vajeeston, P.; Ruud, A.; Drathen, C.; Emerich, H.; Wragg, D. S.; Fjellvåg, H. Bismuth Vanadate and Molybdate: Stable Alloying Anodes for Sodium-Ion Batteries. *Chem. Mater.* **2017**, *29*, 2803−2810.

(11) Su, D.; Wang, G. Single-Crystalline Bilayered V$_2$O$_5$ Nanobelts for High-Capacity Sodium-Ion Batteries. *ACS Nano* **2013**, *7*, 11218−11226.

(12) Ni, J.; Fu, S.; Wu, C.; Maier, J.; Yu, Y.; Li, L. Self-Supported Nanotube Arrays of Sulfur-Doped TiO$_2$ Enabling Ultrastable and Robust Sodium Storage. *Adv. Mater.* **2016**, *28*, 2259−2265.

(13) Sun, W.; Rui, X.; Zhang, D.; Jiang, Y.; Sun, Z.; Liu, H.; Dou, S. Bismuth Sulfide: A High-Capacity Anode for Sodium-Ion Batteries. *J. Power Sources* **2016**, *309*, 135−140.

(14) Park, H.; Choi, S.; Lee, S.-J.; Cho, Y.-G.; Hwang, G.; Song, H.-K.; Choi, N.-S.; Park, S. Design of an Ultra-Durable Silicon-Based Battery Anode Material with Exceptional High-Temperature Cycling Stability. *Nano Energy* **2016**, *26*, 192−199.

(15) Aurbach, D.; Markovsky, B.; Salitra, G.; Markevich, E.; Talyossef, Y.; Koltypin, M.; Nazar, L.; Ellis, B.; Kovacheva, D. Review on Electrode-Electrolyte Solution Interactions, Related to Cathode Materials for Li-Ion Batteries. *J. Power Sources* **2007**, *165*, 491−499.

(16) Tarascon, J.; Armand, M. Issues and Challenges Facing Rechargeable Lithium Batteries. *Nature* **2001**, *414*, 359−367.

(17) Barsoum, M. W.; El-Raghy, T. Synthesis and Characterization of a Remarkable Ceramic: Ti$_3$SiC$_2$. *J. Am. Ceram. Soc.* **1996**, *79*, 1953−1956.

(18) Xu, W.; Pignatello, J. J.; Mitch, W. A. Role of Black Carbon Electrical Conductivity in Mediating Hexahydro-1,3,5-trinitro-1,3,5-triazine (RDX) Transformation on Carbon Surfaces by Sulfides. *Environ. Sci. Technol.* **2013**, *47*, 7129−7136.

(19) Zou, G.; Guo, J.; Liu, X.; Zhang, Q.; Huang, G.; Fernandez, C.; Peng, Q. Hydrogenated Core-Shell MAX@K$_2$Ti$_8$O$_{17}$ Pseudocapacitance with Ultrafast Sodium Storage and Long-Term Cycling. *Adv. Energy Mater.* **2017**, *7*, 1700700−1700708.

(20) Tesfaye, A. T.; Mashtalir, O.; Naguib, M.; Barsoum, M. W.; Gogotsi, Y.; Djenizian, T. Anodized Ti$_3$SiC$_2$ as an Anode Material for Li-Ion Microbatteries. *ACS Appl. Mater. Interfaces* **2016**, *8*, 16670−16676.

(21) Tesfaye, A. T.; Gogotsi, Y.; Djenizian, T. Tailoring the Morphological Properties of Anodized Ti$_3$SiC$_2$ for Better Power Density of Li-Ion Microbatteries. *Electrochem. Commun.* **2017**, *81*, 29−33.

(22) Sun, H.; Mei, L.; Liang, J.; Zhao, Z.; Lee, C.; Fei, H.; Ding, M.; Lau, J.; Li, M.; Wang, C.; et al. Three-Dimensional Holey-Graphene/Niobia Composite Architectures for Ultrahigh-Rate Energy Storage. *Science* **2017**, *356*, 599−604.

(23) Peng, Q.; Guo, J.; Zhang, Q.; Xiang, J.; Liu, B.; Zhou, A.; Liu, R.; Tian, Y. Unique Lead Adsorption Behavior of Activated Hydroxyl Group in Two-Dimensional Titanium Carbide. *J. Am. Chem. Soc.* **2014**, *136*, 4113−4116.

(24) Racault, C.; Langlais, F.; Naslain, R. Solid-State Synthesis and Characterization of the Ternary Phase Ti$_3$SiC$_2$. *J. Mater. Sci.* **1994**, *29*, 3384−3392.

(25) Xu, J.; Zhao, M. Q.; Wang, Y.; Yao, W.; Chen, C.; Anasori, B.; Asia, S.; Ren, C. E.; Mathis, T.; Gomes, L.; et al. Demonstration of Li-Ion Capacity of MAX Phases. *ACS Energy Lett.* **2016**, *1*, 1094−1099.

(26) Ni, J.; Fu, S.; Wu, C.; Zhao, Y.; Maier, J.; Yu, Y.; Li, L. Superior Sodium Storage in Na$_2$Ti$_3$O$_7$ Nanotube Arrays through Surface Engineering. *Adv. Energy Mater.* **2016**, *6*, 1502568−1502575.

(27) Li, Z.; Shen, W.; Wang, C.; Xu, Q.; Liu, H.; Wang, Y.; Xia, Y. Ultra-Long Na$_2$Ti$_3$O$_7$ Nanowires@Carbon Cloth as a Binder-Free Flexible Electrode with a Large Capacity and Long Lifetime for Sodium-Ion Batteries. *J. Mater. Chem. A* **2016**, *4*, 17111−17120.

(28) Rudola, A.; Saravanan, K.; Devaraj, S.; Gong, H.; Balaya, P. Na$_2$Ti$_6$O$_{13}$: A Potential Anode for Grid-Storage Sodium-Ion Batteries. *Chem. Commun.* **2013**, *49*, 7451−7453.

(29) Senguttuvan, P.; Rousse, G.; Seznec, V.; Tarascon, J.-M.; Palacín, M. R. Na$_2$Ti$_3$O$_7$: Lowest Voltage Ever Reported Oxide

Insertion Electrode for Sodium Ion Batteries. *Chem. Mater.* **2011**, *23*, 4109−4111.

(30) Cao, K.; Jiao, L.; Pang, W. K.; Liu, H.; Zhou, T.; Guo, Z.; Wang, Y.; Yuan, H. $Na_2Ti_6O_{13}$ Nanorods with Dominant Large Interlayer Spacing Exposed Facet for High-Performance Na-Ion Batteries. *Small* **2016**, *12*, 2991−2997.

(31) Zhang, Y.; Foster, C. W.; Banks, C. E.; Shao, L.; Hou, H.; Zou, G.; Chen, J.; Huang, Z.; Ji, X. Graphene-Rich Wrapped Petal-Like Rutile TiO_2 Tuned by Carbon Dots for High-Performance Sodium Storage. *Adv. Mater.* **2016**, *28*, 9391−9399.

(32) Tao, D.; Fang, Z.; Qiu, M.; Li, Y.; Huang, X.; Ding, K.; Chen, W.; Su, W.; Zhang, Y. First-Principles Study of $Na_{2+x}Ti_7O_{15}$ as Anode Materials for Sodium-Ion Batteries. *J. Alloys Compd.* **2016**, *689*, 805−811.

(33) Liu, Y.; Zhang, N.; Yu, C.; Jiao, L.; Chen, J. $MnFe_2O_4$@C Nanofibers as High-Performance Anode for Sodium-Ion Batteries. *Nano Lett.* **2016**, *16*, 3321−3328.

(34) Augustyn, V.; Come, J.; Lowe, M. A.; Kim, J. W.; Taberna, P. L.; Tolbert, S. H.; Abruña, H. D.; Simon, P.; Dunn, B. High-Rate Electrochemical Energy Storage Through Li^+ Intercalation Pseudocapacitance. *Nat. Mater.* **2013**, *12*, 518−522.

(35) Chen, C.; Wen, Y.; Hu, X.; Ji, X.; Yan, M.; Mai, L.; Hu, P.; Shan, B.; Huang, Y. Na^+ Intercalation Pseudocapacitance in Graphene-Coupled Titanium Oxide Enabling Ultra-Fast Sodium Storage and Long-Term Cycling. *Nat. Commun.* **2015**, *6*, 6929−6936.

(36) Wang, J.; Polleux, J.; Lim, J.; Dunn, B. Pseudocapacitive Contributions to Electrochemical Energy Storage in TiO_2 (Anatase) Nanoparticles. *J. Phys. Chem. C* **2007**, *111*, 14925−14931.

(37) Kim, J. W.; Augustyn, V.; Dunn, B. The Effect of Crystallinity on the Rapid Pseudocapacitive Response of Nb_2O_5. *Adv. Energy Mater.* **2012**, *2*, 141−148.

(38) Kim, K. T.; Ali, G.; Chung, K. Y.; Yoon, C. S.; Yashiro, H.; Sun, Y. K.; Lu, J.; Amine, K.; Myung, S. T. Anatase Titania Nanorods as an Intercalation Anode Material for Rechargeable Sodium Batteries. *Nano Lett.* **2014**, *14*, 416−422.

(39) Ryu, W. H.; Wilson, H.; Sohn, S.; Li, J.; Tong, X.; Shaulsky, E.; Schroers, J.; Elimelech, M.; Taylor, A. D. Heterogeneous WS_x/WO_3 Thorn-Bush Nanofiber Electrodes for Sodium-Ion Batteries. *ACS Nano* **2016**, *10*, 3257−3266.

(40) Nakai, H.; Kubota, T.; Kita, A.; Kawashima, A. Investigation of the Solid Electrolyte Interphase Formed by Fluoroethylene Carbonate on Si Electrodes. *J. Electrochem. Soc.* **2011**, *158*, A798−A801.

(41) Choi, S.; Cho, Y.; Kim, J.; Choi, N.; Song, H.; Wang, G.; Park, S. Mesoporous Germanium Anode Materials for Lithium-Ion Battery with Exceptional Cycling Stability in Wide Temperature Range. *Small* **2017**, *13*, 1603045−1603054.

(42) Zou, G.; Guo, J.; Peng, Q.; Zhou, A.; Zhang, Q.; Liu, B. Synthesis of Urchin-Like Rutile Titania Carbon Nanocomposites by Iron-Facilitated Phase Transformation of MXene for Environmental Remediation. *J. Mater. Chem. A* **2016**, *4*, 489−499.

Heterogeneous Ti_3SiC_2@ C-Containing $Na_2Ti_7O_{15}$ Architecture for High-Performance Sodium Storage at Elevated Temperatures

Guodong Zou[1], Qingrui Zhang[2], Carlos Fernandez[3], Gang Huang[4], Jianyu Huang[1] and Qiuming Peng*[1]

[1]State Key Laboratory of Metastable Materials Science and Technology, Yanshan University, Qinhuangdao 066004, China

[2]Hebei Key Laboratory of Applied Chemistry, School of Environmental and Chemical Engineering, Yanshan University, Qinhuangdao 066004, China

[3]School of Pharmacy and Life Sciences, Robert Gordon University, Aberdeen, AB107GJ, UK

[4]WPI Advanced Institute for Materials Research, Tohoku University, Sendai 980-8577, Japan

Table S1. Chemical compositions of three samples based on ICP analysis.

Samples	Elemental composition (mg/L)			$Na_2Ti_7O_{15}$ concentration (wt.%)
	Ti	Si	Na	
C-NTO10	68.43	10.31	1.95	26.38
C-NTO30	65.71	8.36	2.98	40.31
C-NTO60	65.11	7.88	3.24	43.68

Table S2. Chemical compositions of three samples in terms of EDX analysis.

Samples	Elemental percentage (wt.%)					$Na_2Ti_7O_{15}$ concentration (wt. %)
	Ti	Si	Na	C	O	
C-NTO10	68.49	10.34	1.93	9.16	10.08	26.12
C-NTO30	65.61	8.36	2.97	7.55	15.51	40.16
C-NTO60	65.01	7.85	3.25	6.95	16.94	43.92

Table S3. Electrochemical properties of titanium-based anode materials for sodium ion battery at 25°C reported to date.

	Anode materials	Current density (mA g⁻¹)	Cycle number	Capacity (mAh g⁻¹)	Ref.
Titanium dioxides	Graphene−rutile TiO_2	83.75	300	245	S1
		837.5	1100	144	
		3350	4000	59	
	TiO_2/graphene	12000	4000	90	S2
	B-doped TiO_2	660	400	140	S3
Titanium-based MXenes	Ti_2CT_x	20	100	175	S4
	$Ti_3C_2T_x$	200	1000	65	S5
		50	100	100	
	$Ti_3C_2T_x$/CNT-SA	20	100	179	S6
Layered titanium-based oxides	$Na_{0.66}[Li_{0.22}Ti_{0.78}]O_2$	212	1200	75	S7
	$NaTiO_2$	20	60	152	S8
	$Na_{2/3}Ni_{1/6}Mg_{1/6}Ti_{2/3}O_2$	9.6	100	92	S9
	$Na_{2/3}Co_{1/3}Ti_{2/3}O_2$	200	1200	65	S10
		500	3000	45	
	$Na_{0.62}Ti_{0.37}Cr_{0.63}O_2$	500	1000	50	S11
	$Na_{0.6}Ni_{0.3}Ti_{0.7}O_2$	550	50	80	S12
Spinel $Li_4Ti_5O_{12}$	$Li_4Ti_5O_{12}$	17.5	50	170	S13
	Cu-doped $Li_4Ti_5O_{12}$/C nanofiber	30	150	148	S14
		400	150	75	
Titanium phosphates	$KTi_2(PO_4)_3$/Carbon	640	1200	90	S15
		2560	5000	69	
	$NaTi_2(PO_4)_3$@Graphene	133	200	112	S16
		1330	1000	75	
	$NaTi_2(PO_4)_3$ nanocubes	133	1000	100	S17
		1330	10000	80	
	Carbon-coated $NaTi_2(PO_4)_3$ microflowers	133	200	125	S18
		665	500	117	
		2660	10000	85	
Potassium titanate	Tunnel-Structured K_xTiO_2 Nanorods	200	1000	105	S19
	$K_2Ti_6O_{13}$ nanowires	400	200	99	S20
	MAX@H-$K_2Ti_8O_{17}$	200	200	189	S21
		1000	1000	145	
		10000	10000	75	
Sodium titanate	Hydrogenated $Na_2Ti_3O_7$ Nanoarrays	177	200	190	S22
		6200	10000	65	
	$Na_2Ti_3O_7$/C Textiles	1000	1000	130	S23
	$Na_2Ti_6O_{13}$ nanorods	100	300	172	S24

	400	800	129	
Na$_2$Ti$_3$O$_7$/VS$_2$	20	50	293	S25
	200	100	203	
Na$_2$Ti$_3$O$_7$ /rGO	100	300	133	S26
Surface engineered	885	1200	90	S27
Na$_2$Ti$_3$O$_7$	1770	10000	78	
Na$_2$Ti$_6$O$_{13}$–graphite	4000	5000	17	S28
NTO nanotube arrays	100	200	145	S29
	200	200	120	
	400	5000	55	
Na$_2$Ti$_3$O$_7$ nanotubes	400	100	185	S30
	500	500	110	
Na$_2$Ti$_7$O$_{15}$	1000	200	130	S31
Na$_2$Ti$_3$O$_7$@C HHSs	8800	1000	68	S32
Na$_2$Ti$_3$O$_7$ microflowers	400	1100	85	S33
C-NTO-30	**200**	**200**	**196**	**This work**
	1000	**200**	**152**	
	6000	**1000**	**112**	
	10000	**10000**	**93**	

Table S4. Electrochemical properties of reported anode materials for Sodium/Lithium ion batteries at elevated temperatures.

Anode materials	Current density (mA g^{-1})	Cycle number	Operating temperature (^{o}C)	Battery type	Capacity retention (%)	Average fading percentage	Ref.
Hierarchically Porous Li$_4$Ti$_5$O$_{12}$	175	100	40	SIBs	70	0.3	S34
Phosphorus-Graphene Nanosheet Hybrids	260	200	60	LIBs	73	0.135	S35
Si@BaTiOx-600 nanoparticles	3579	500	60	LIBs	64	0.072	S36
mesoporous Ge particles	600	300	60	LIBs	84	0.053	S37
C-NTO-30	10000	10000	40	SIBs	81	0.0019	This work
	200	200	60		87	0.065	
	10000	3000			75	0.008	
	10000	1000	80		60	0.04	

Notes: Average fading percentage was equal to (1-capacity retention (%))/cycle number.

Table S5. The fitted data based on the EIS curves.

Samples	R_s (ohm)	R_{ct} (ohm)	Z_W
C-NTO10	6.571	81.6	0.808
C-NTO30	6.674	101.64	0.8244
C-NTO60	8.999	684.4	0.8644
C-NTO30-60℃	3.192	39.37	0.7623
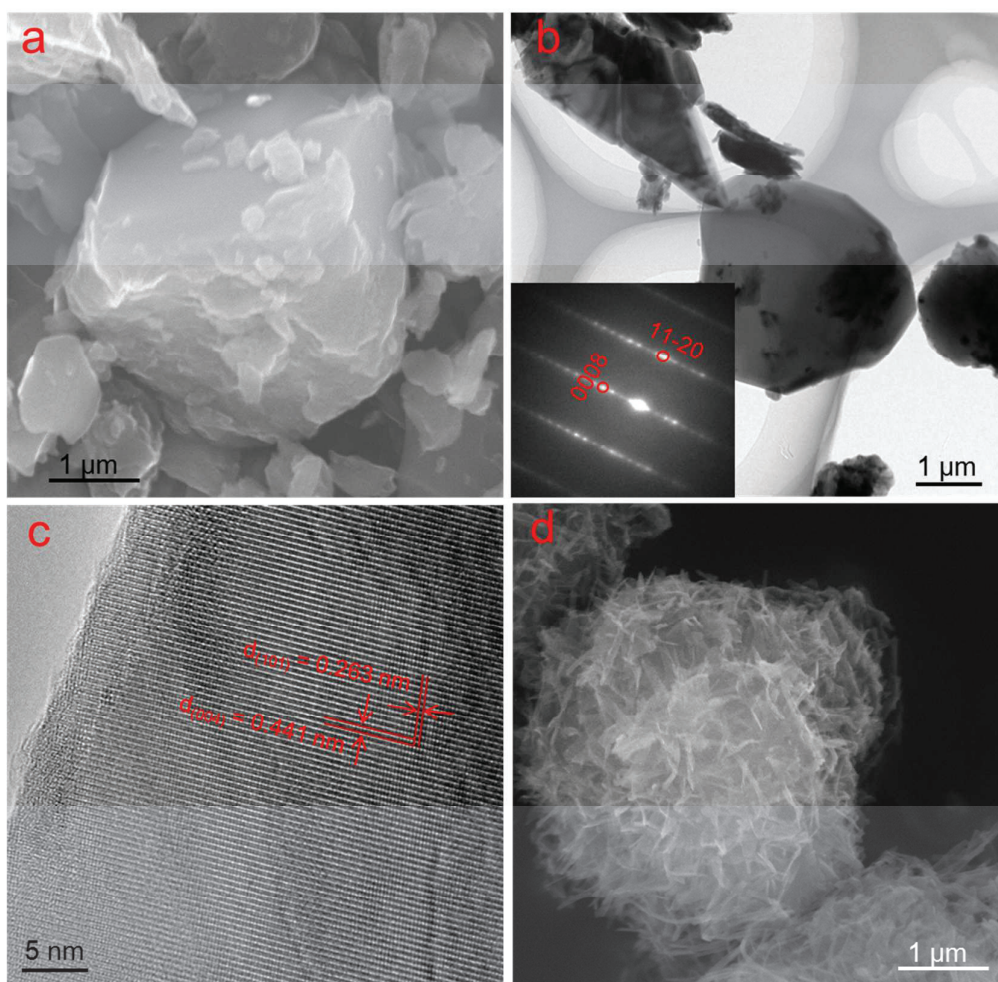
Figure S1. (a) Typical SEM image of TSC. (b) Typical TEM image of TSC. The inset is the corresponding selected area electron diffraction (SAED) of TSC. (c) HRTEM image of TSC (d) Typical SEM image of the sample which is prepared by microwave-assisted in 2 M NaOH for 10 min.
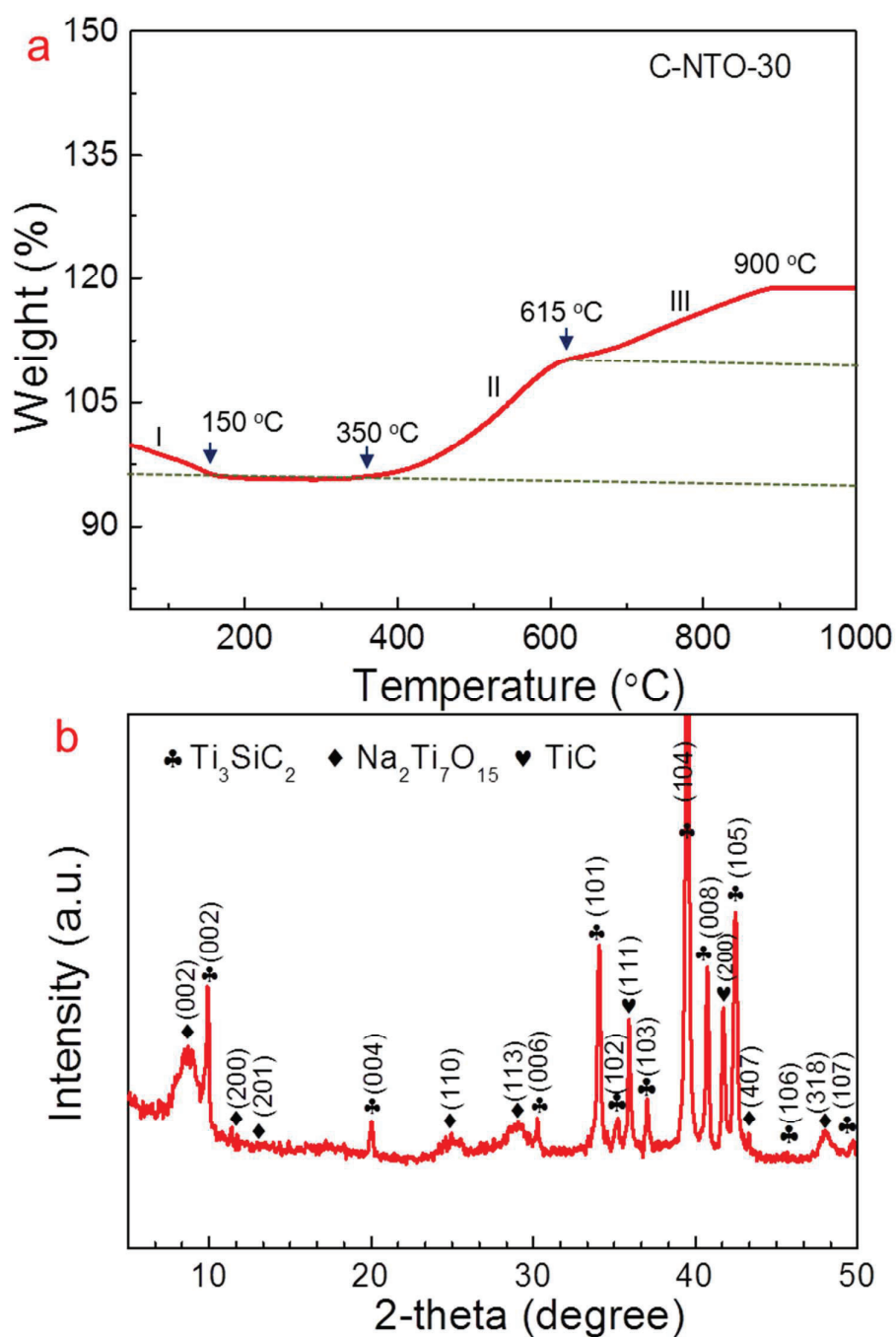
Figure S2. (a) The TG curve of the C-NTO30 sample at a heat rate of 5 ^{o}C/min. The I step is the dehydration process, the II and III steps are related to the two-step oxidation of TSC, respectively.[S38] (b) Typical XRD pattern of the C-NTO30 sample after annealing at 150 ^{o}C for 30 min.
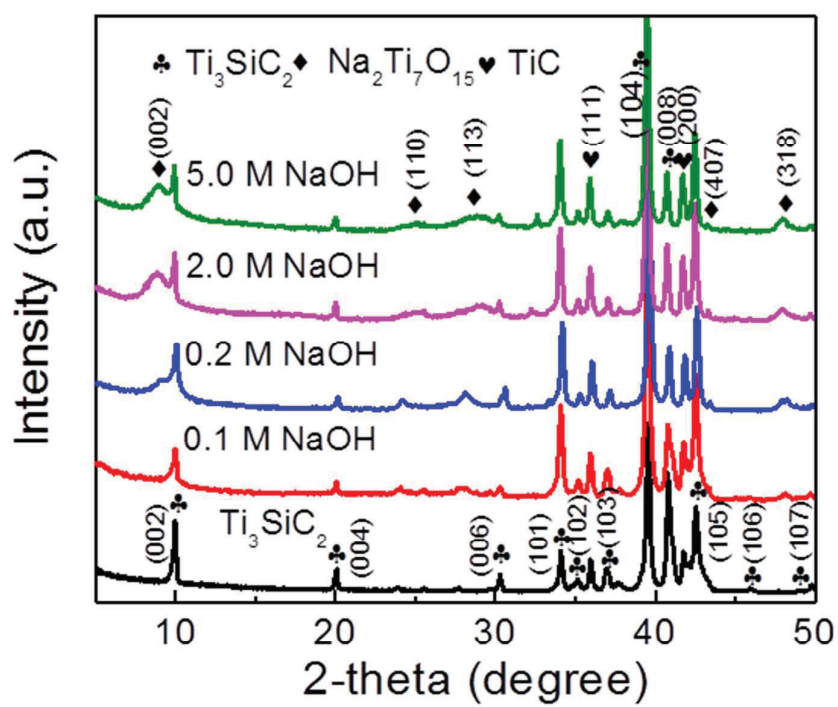
Figure S3. The effect of NaOH concentration on the formation of NTO (200 ^{o}C, 30 min)
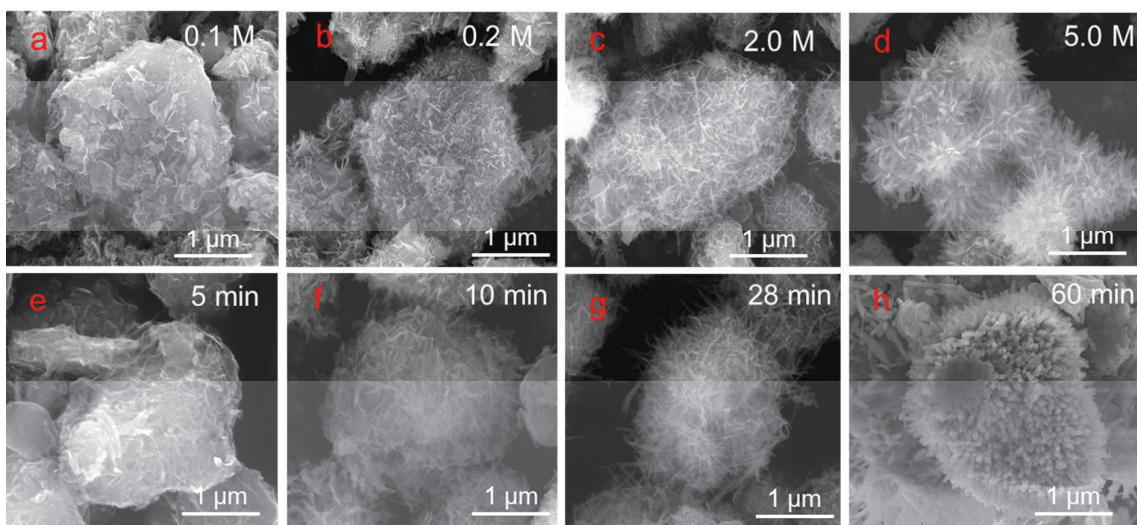
Figure S4. The effect of NaOH concentration on NTO morphology evolution (200 ^{o}C, 30 min), (a) 0.1 M, (b) 0.2 M, (c) 2.0 M and (d) 5.0 M. The effect of incubation time on NTO morphology evolution (2.0 M NaOH, 200 ^{o}C), (e) 5 min, (f) 10 min, (g) 28 min and (h) 60 min.
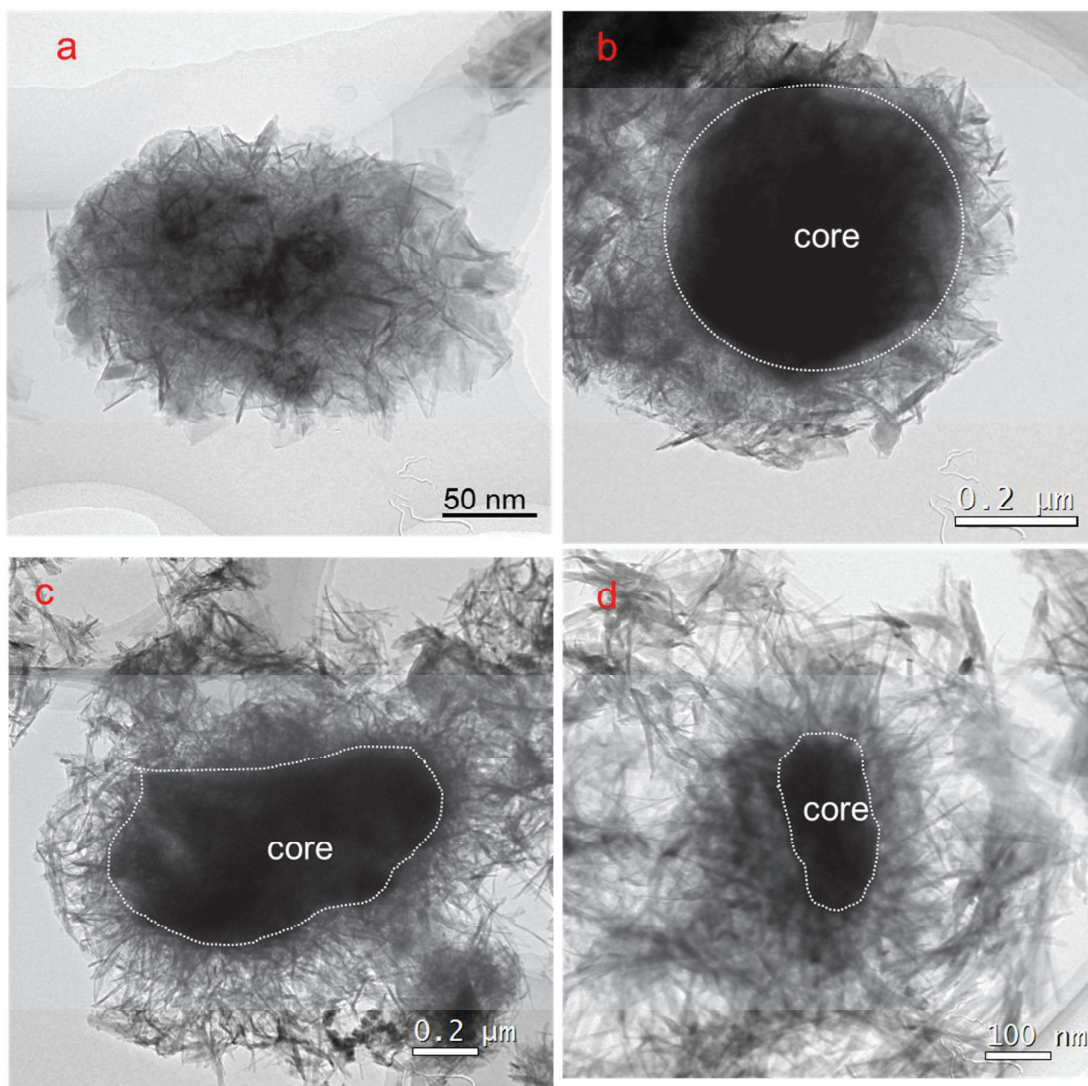
Figure S5. (a) TEM images of the sample after incubating for 30 min in 5.0 M NaOH. The core is hardly detected and the concentration of C-NTO is about 91 %. TEM images of MAX@C-NTO samples after incubating different times in 2.0 M NaOH. (b) 6 min, (c) 10 min, (d) 60 min.
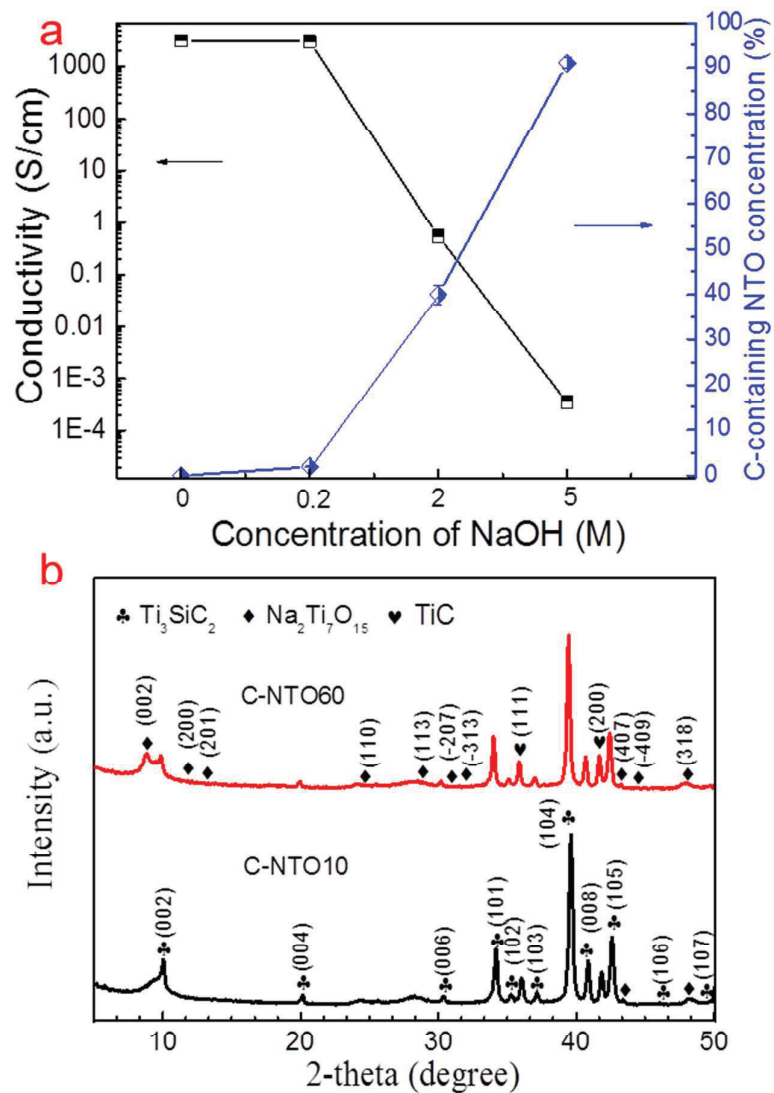
Figure S6. (a) The conductivity of the samples prepared in different NaOH concentrations (200 ^{o}C, 30 min). (b) The typical XRD patterns of the C-NTO60 and C-NTO10 samples (2.0 M NaOH, 200 ^{o}C).
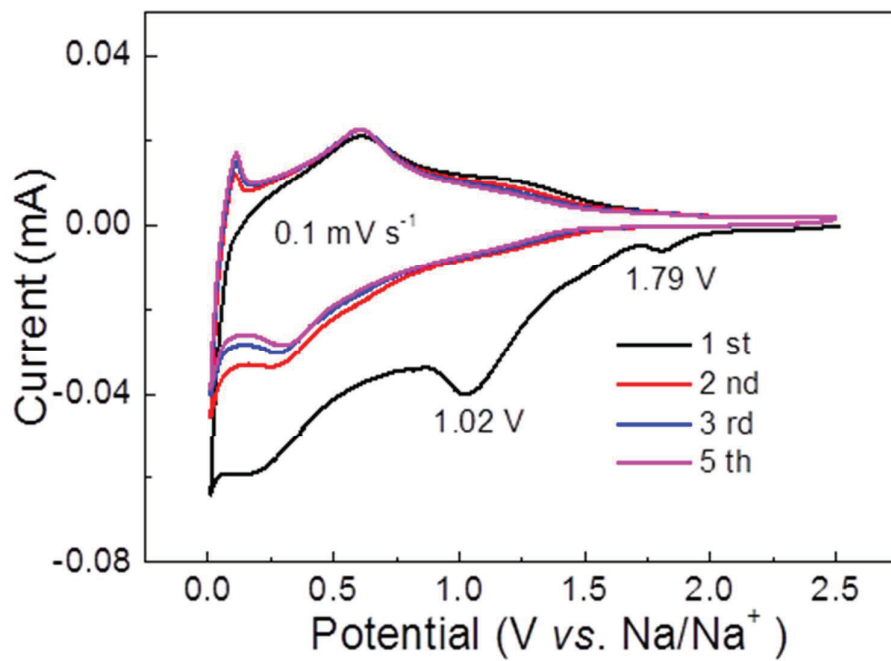
Figure S7. CV curves of the C-NTO30 recorded at a scan rate of 0.1 mV s^{-1} over a voltage range of 0.01–2.5 V *versus* Na/Na$^+$ without a presodiation treatment.
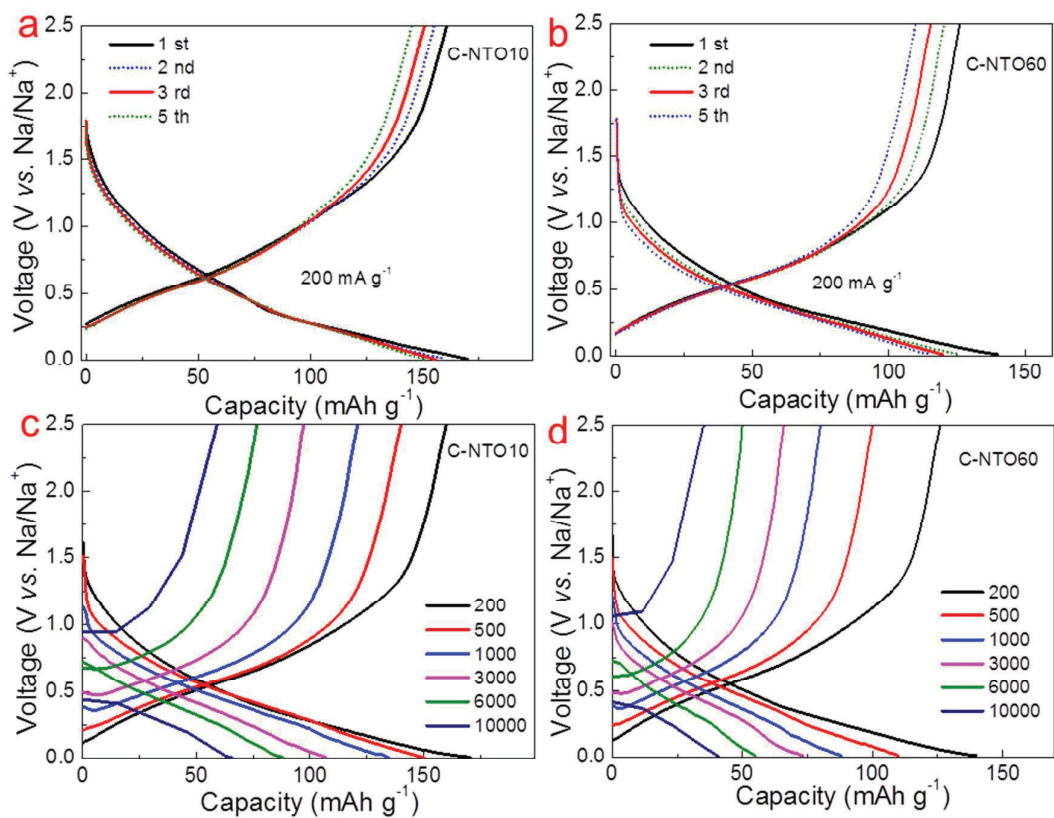
Figure S8. The charge-discharge curves at a current density of 200 mA g^{-1} during initial cycles, (a) C-NTO10; (b) C-NTO60. First charge-discharge profiles at different current rates, (c) C-NTO10; (d) C-NTO60.
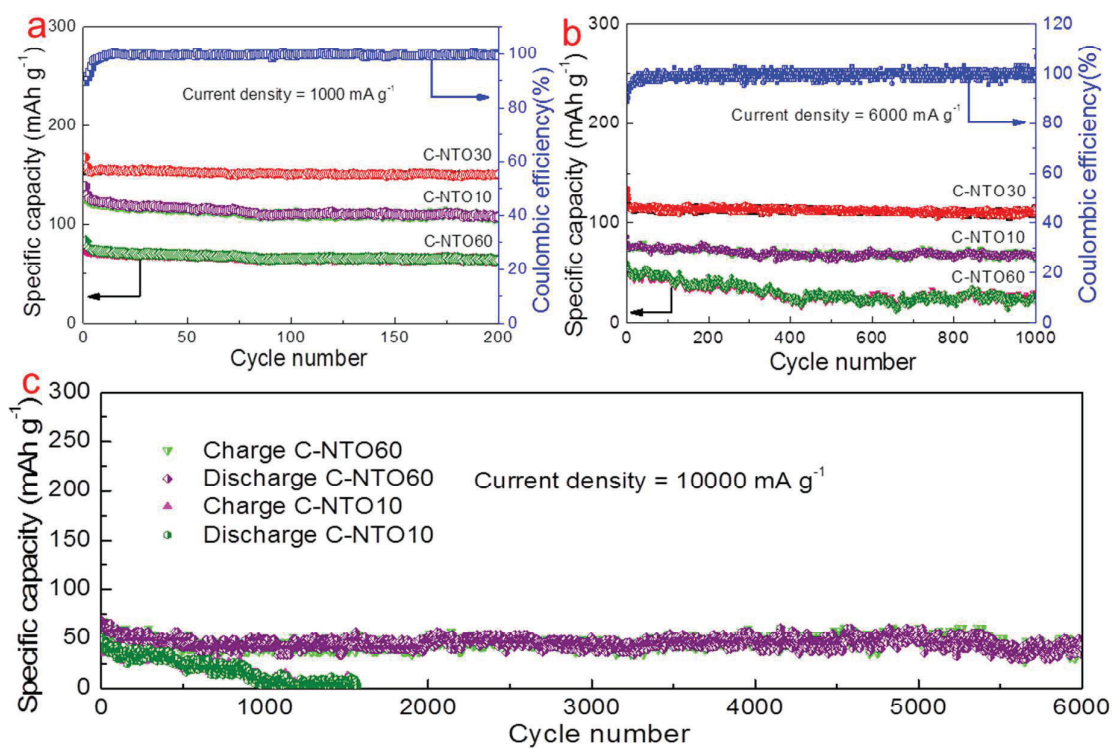
Figure S9. Cycle performance of C-NTO samples after incubating time at different current

densities, (a) 1000 mA g^{-1},(b) 6000 mA g^{-1}. (c) Cycle performance of the C-NTO10 and

C-NTO60 samples at a current density of 10000 mA g^{-1}.
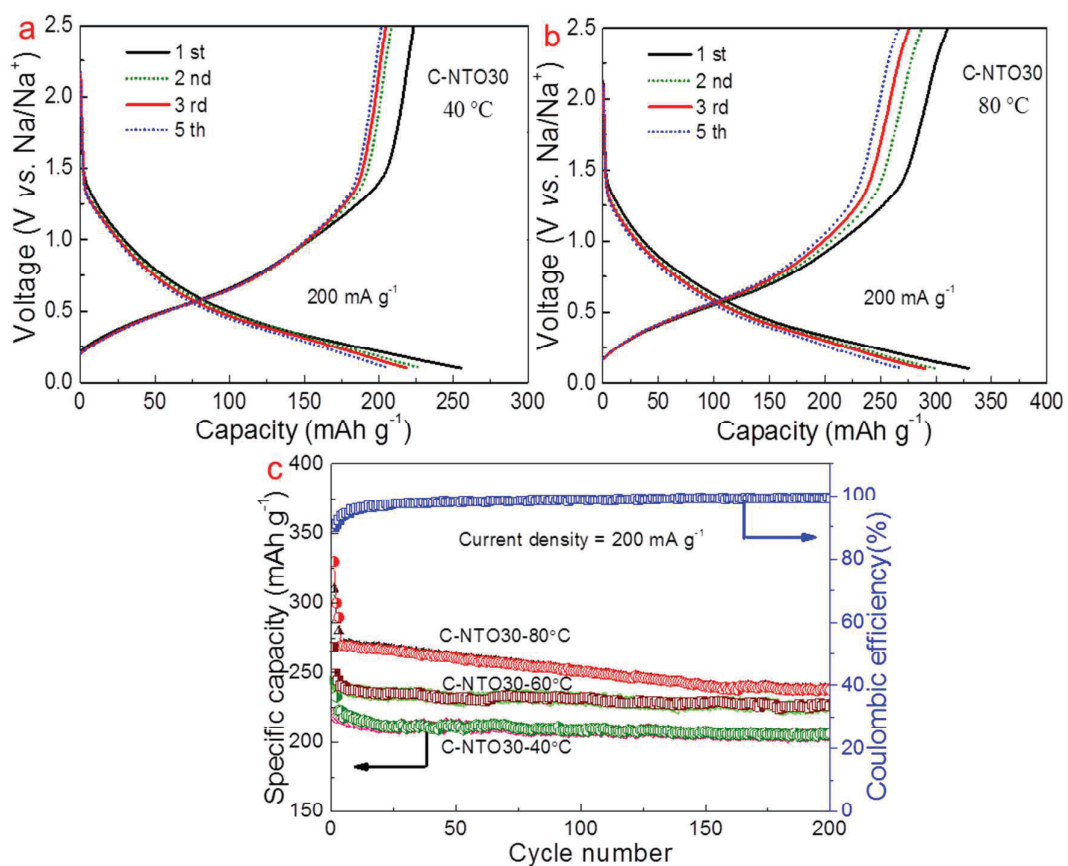
Figure S10. Initial charge-discharge profiles with a current density of 200 mA g^{-1}, (a) the

C-NTO30-40 ^{o}C sample and (b) the C-NTO30-80 ^{o}C sample. (c) Cycle properties of the

C-NTO30-40 ^{o}C, C-NTO30-60 ^{o}C and C-NTO30-80 ^{o}C samples at a current density of 200

mA g^{-1}, and the corresponding Coulombic efficiency of C-NTO30-60 ^{o}C sample.
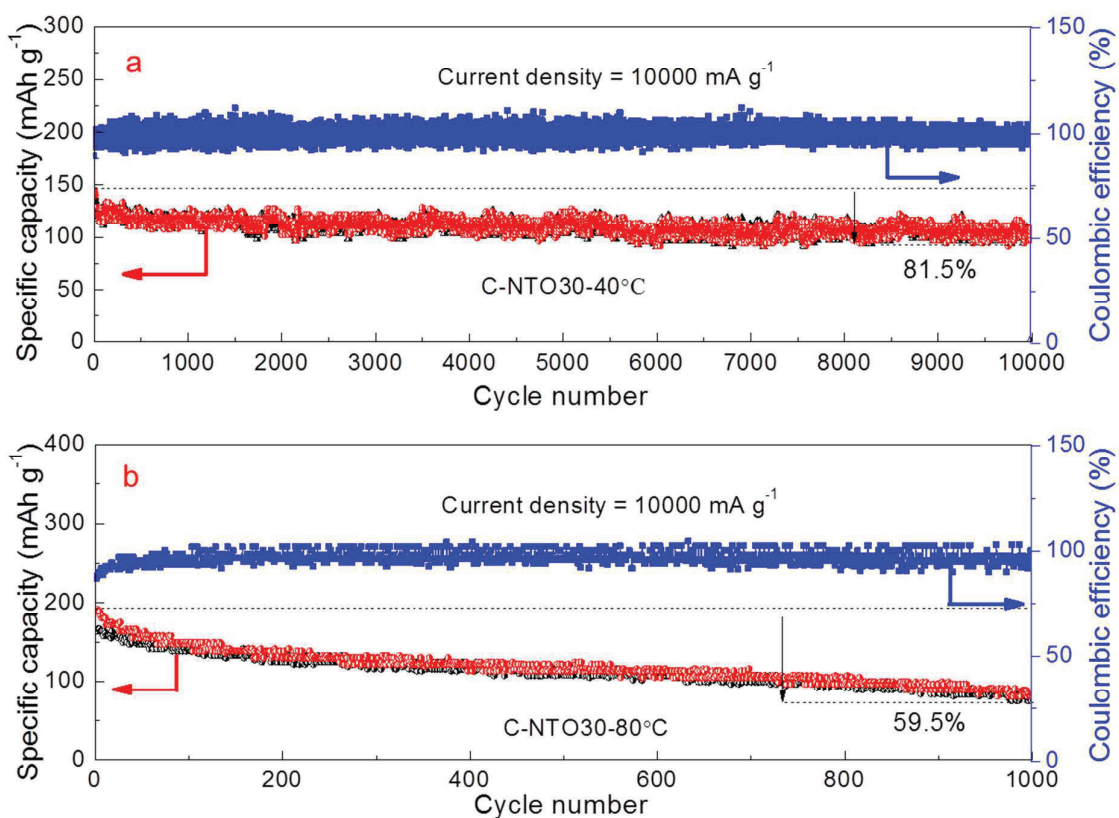
Figure 11 Cycling properties of the electrodes at a current rate of 10000 mA g^{-1}. (a) The C-NTO30-40°C, a capacity retention is 81.5% after 10000 cycles. (b) The C-NTO30-80°C, a capacity retention is 59.5% after 1000 cycles.
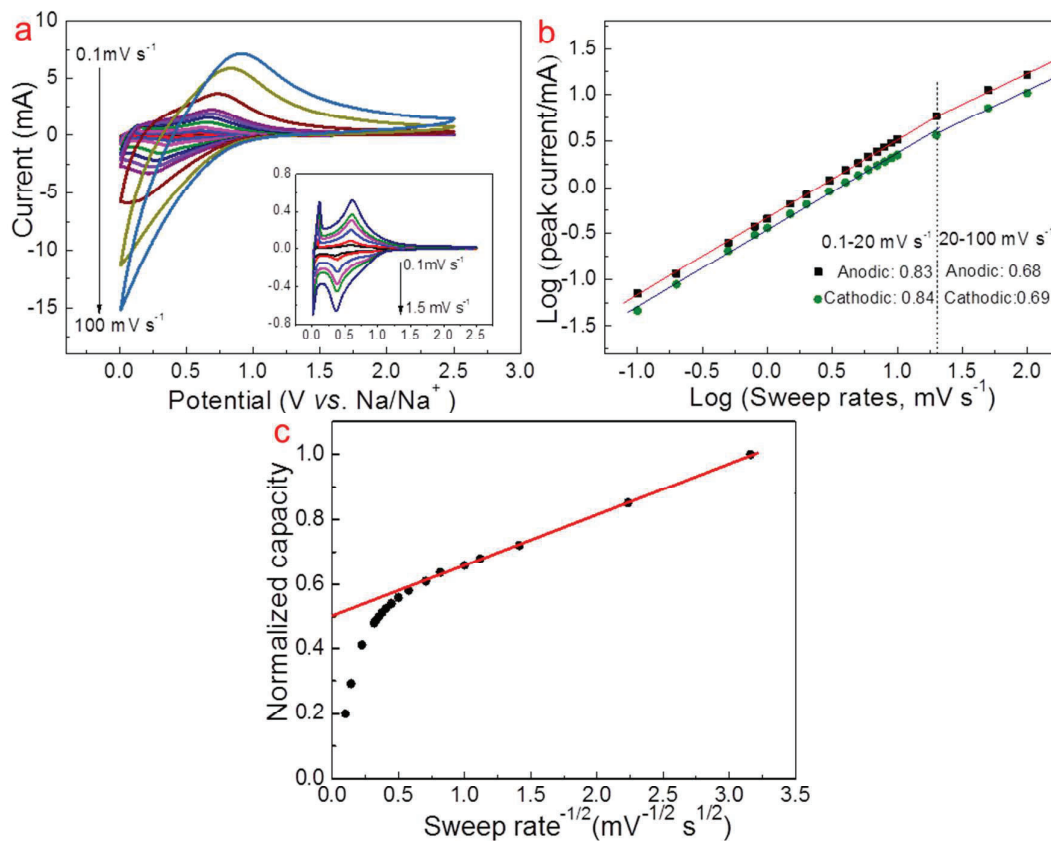
Figure S12. (a) Cyclic voltammetry curves of the C-NTO30-60°C electrode in sweep rate range from 0.1 to 100 mV s^{-1}. (b) b-value determined by the relationship between the peak currents and the sweep rates. (c) The normalized capacity *versus* sweep rate$^{-1/2}$.
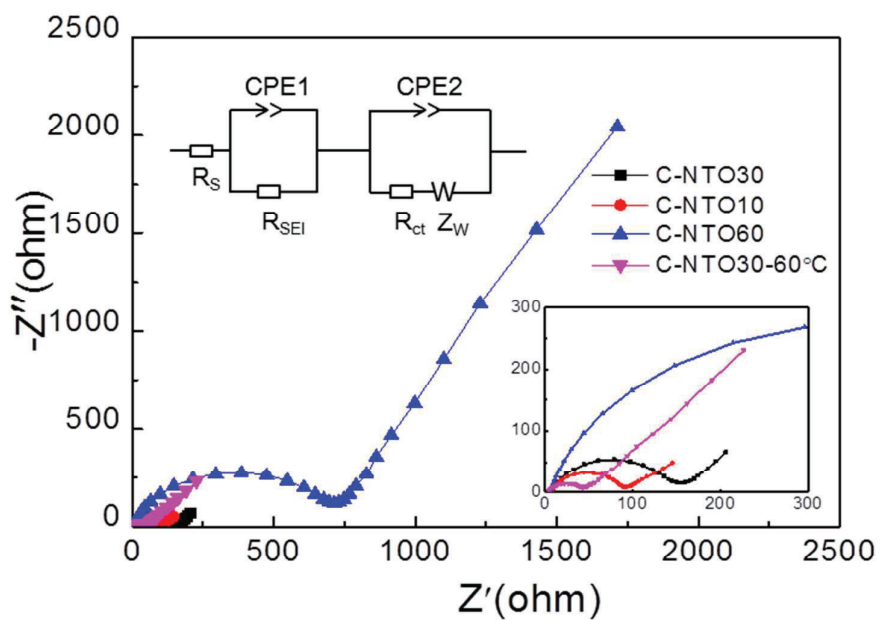
Figure S13. EIS of different samples after 1st cycle. The inset corresponds to the fitted circuit.

The down inset assigns to the local magnification of the EIS curves.
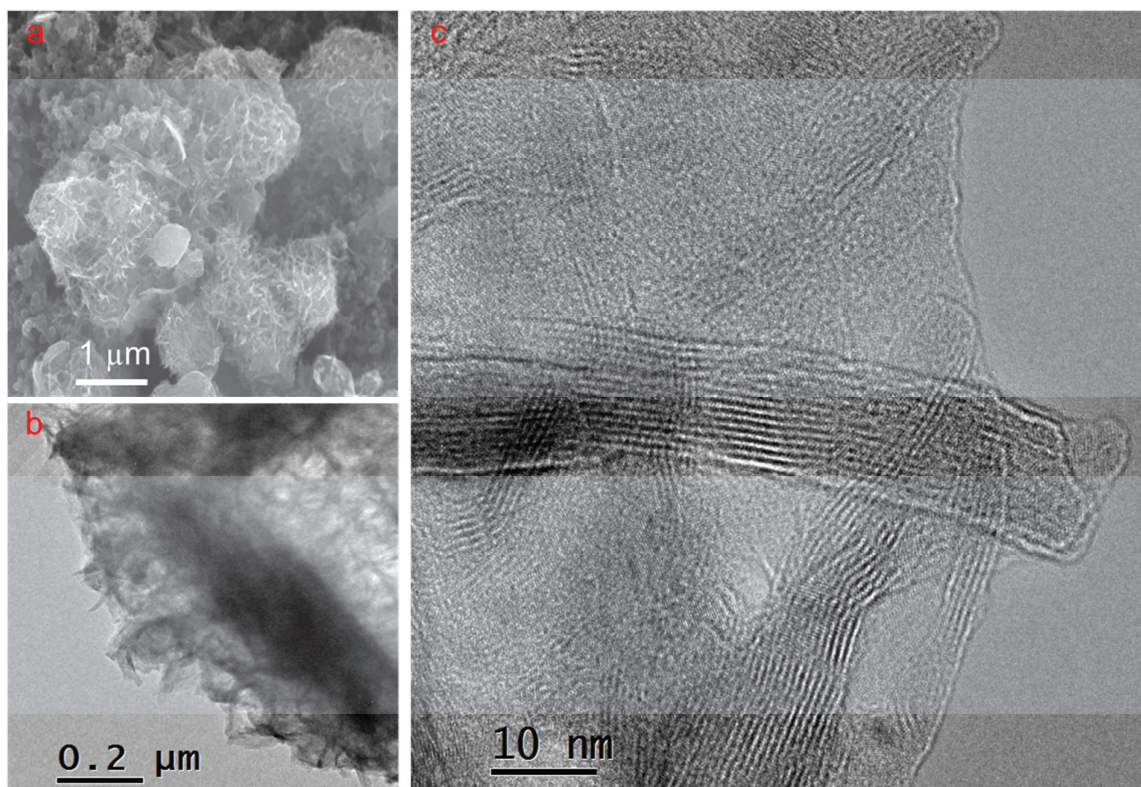
Figure S14. Microstructure of the C-NTO30-60 ^{o}C samples after 500 cycles. (a) SEM image.

(b) TEM image. (c) HRTEM image of the shell.
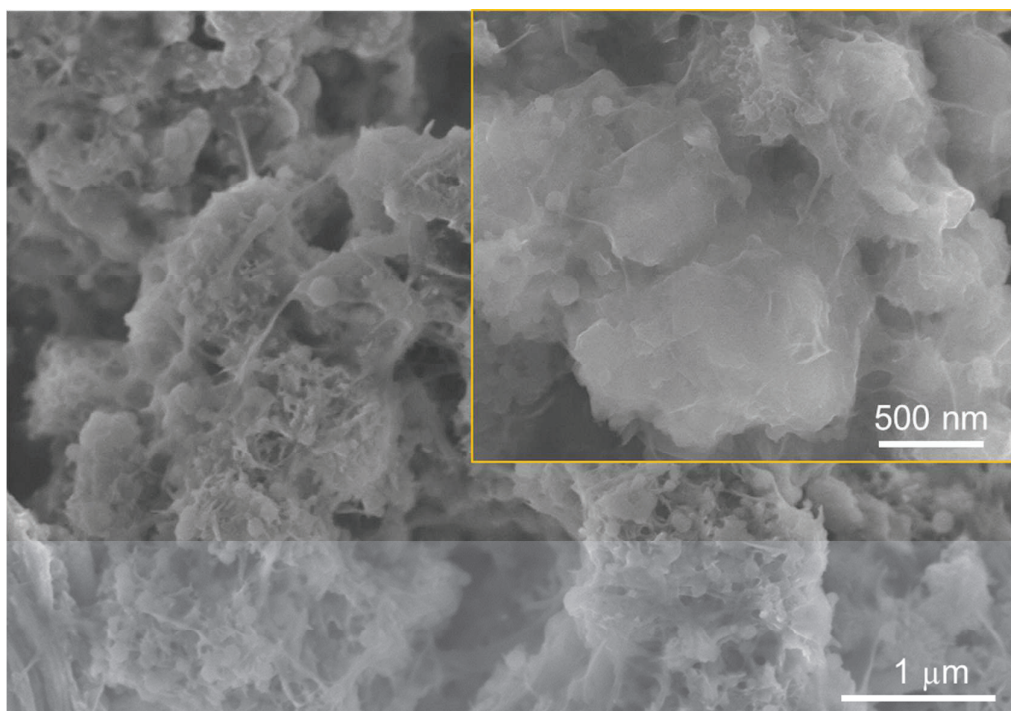
Figure S15. Typical SEM images of the C-NTO30-80 $^{\circ}$C samples after 1000 cycles. The obvious aggregation occurred. The inset corresponds to the local high magnification image.
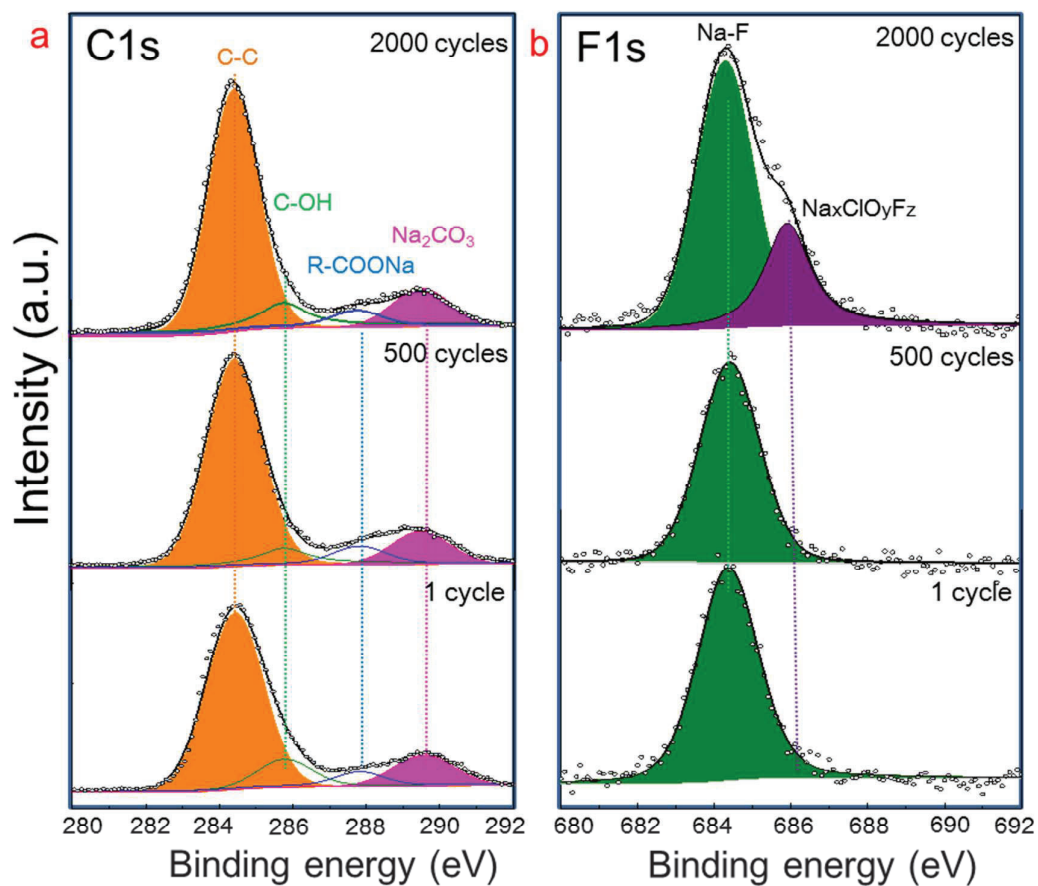
Figure S16. *Ex situ* XPS profiles of the C-NTO30-60 $^{\circ}$C sample after different cycles. (a) C1s spectrum. Both C-OH and Na_2CO_3 peaks remain stable with increasing cycle number. (b) F1s spectrum. A new $Na_xClO_yF_z$ peaks is detected after 2000 cycles.
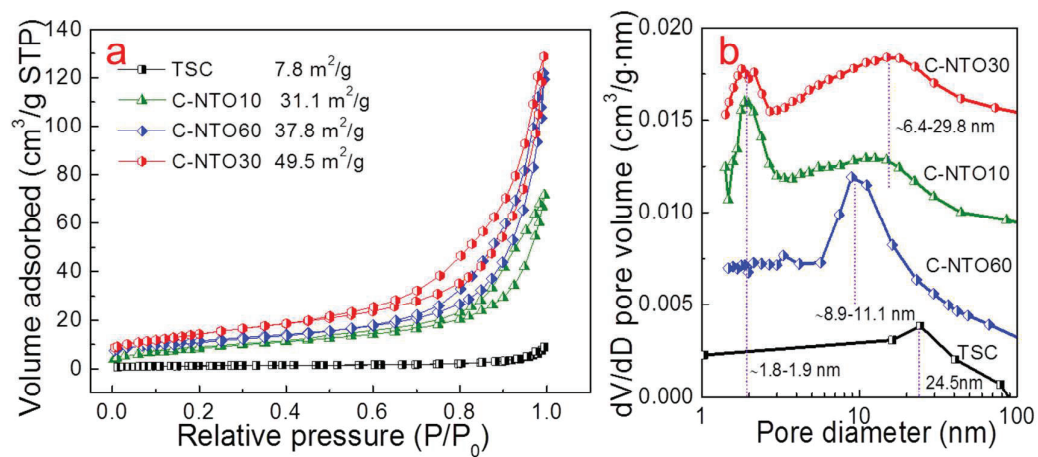
Figure S17 (a) Nitrogen adsorption-desorption isotherms and (b) the pore size distribution of

the TSC and different state C-NTO samples.

REFERENCES

S1. Zhang, Y.; Foster, C.; Banks, C.; Shao, L.; Hou, H.; Zou, G.; Chen, J.; Huang, Z.; Ji, X. Graphene-Rich Wrapped Petal-Like Rutile TiO_2 Tuned by Carbon Dots for High-Performance Sodium Storage. *Adv. Mater.* **2016**, *28*, 9391-9399.

S2. Chen, C.; Wen, Y.; Hu, X.; Ji, X.; Yan, M.; Mai, L.; Hu, P.; Shan, B.; Huang,Y. Na^+ Intercalation Pseudocapacitance in Graphene-Coupled Titanium Oxide Enabling Ultra-Fast Sodium Storage and Long-Term Cycling. *Nat. Commun.* **2015**, *6*, 6929-6936.

S3. Wang, B.; Zhao, F.; Du, G.; Porter, S.; Liu, Y.; Zhang, P.; Cheng, Z.; Liu, H.; Huang, Z. Boron-Boped Anatase TiO_2 as a High-Performance Anode Material for Sodium-Ion Batteries. *ACS Appl. Mater. Interfaces* **2016**, *8*, 16009-16015.

S4. Wang, X.; Kajiyama, S.; Iinuma, H.; Hosono, E.; Oro, S.; Moriguchi, I.; Okubo, M.; Yamada, A. Pseudocapacitance of MXene Nanosheets for High-Power Sodium-Ion Hybrid Capacitors. *Nat. Commun.* **2015**, *6*, 6544-6549.

S5. Wang, X.; Shen, X.; Gao, Y.; Wang, Z.; Yu, R.; Chen, L. Atomic-Scale Recognition of Surface Structure and Intercalation Mechanism of Ti_3C_2X. *J. Am. Chem. Soc.* **2015**, *137*, 2715-2721.

S6. Xie, X.; Zhao, M. Q.; Anasori, B.; Maleski, K.; Ren, C. E.; Li, J.; Byles, B.; Pomerantseva, E.; Wang, G.; Gogotsi, Y. Porous Heterostructured MXene/Carbon Nanotube Composite Paper with High Volumetric Capacity for Sodium-Based Energy Storage Devices. *Nano Energy* **2016**, *26*, 513-523.

S7. Wang, Y.; Yu, X.; Xu, S.; Bai, J.; Xiao, R.; Hu, Y.; Li, H.; Yang, X.; Chen, L.; Huang, X. A Zero-Strain Layered Metal Oxide as the Negative Electrode for Long-Life Sodium-Ion Batteries. *Nat. Commun.* **2013**, *4*, 2365-2371.

S8. Wu, D.; Li, X.; Xu, B.; Twu, N.; Liu, L.; Ceder, G. NaTiO$_2$: A Layered Anode Material for Sodium-Ion Batteries. *Energy Environ. Sci.* **2015**, *8*,195-202.

S9. Wang, P.; Yao, H.; Zuo, T.; Yin, Y.; Guo, Y. Novel P2-Type Na$_{2/3}$ Ni$_{1/6}$ Mg$_{1/6}$ Ti$_{2/3}$ O$_2$ as an Anode Material for Sodium-Ion Batteries. *Chem. Commun.* **2017**, *53*, 1957-1960.

S10. Yu, H.; Ren, Y.; Xiao, D.; Guo, S.; Zhu, Y.; Qian, Y.; Gu, L.; Zhou, H. An Ultrastable Anode for Long-Life Room-Temperature Sodium-Ion Batteries. *Angew. Chem. Int. Ed.* **2014**, *53*, 8963-8969.

S11. Guo, S.; Sun, Y.; Yi, J.; Zhu, K.; Liu, P.; Zhu, Y.; Zhu, G.; Chen, M.; Ishida, M.; Zhou, H. Understanding Sodium-Ion Diffusion in Layered P2 and P3 Oxides *via* Experiments and First-Principles Calculations: A Bridge Between Crystal Structure and Electrochemical Performance. *NPG Asia Mater.* **2016**, *8*, e266-e275.

S12. Fielden, R.; Obrovac, M. Low Voltage Sodium Intercalation in Na$_x$Ni$_{x/2}$Ti$_{1-x/2}$O$_2$ ($0.5 \leq$ x≤ 1.0). *J. Electrochem. Soc*. **2014**, *161*, A1158-A1163.

S13. Sun, Y.; Zhao, L.; Pan, H.; Lu, X.; Gu, L.; Hu, Y.; Li, H.; Armand, M.; Ikuhara, Y.; Chen, L.; *et al*. Direct Atomic-Scale Confirmation of Three-Phase Storage Mechanism in Li$_4$Ti$_5$O$_{12}$ Anodes for Room-Temperature Sodium-Ion Batteries. *Nat. Commun.* **2013**, *4*, 1870-1879.

S14. Ge, Y.; Jiang, H.; Fu, K.; Zhang, C.; Zhu, J.; Chen, C.; Lu, Y.; Qiu, Y.; Zhang, X. Copper-Doped Li$_4$Ti$_5$O$_{12}$/Carbon Nanofiber Composites as Anode for High-Performance Sodium-Ion Batteries. *J. Power Sources* **2014**, *272*, 860-865.

S15. Sheng, J.; Peng, C.; Xu, Y.; Lyu, H.; Xu, X.; An, Q.; Mai, L. KTi$_2$(PO$_4$)$_3$ with Large Ion Diffusion Channel for High-Efficiency Sodium Storage. *Adv. Energy Mater.* **2017**, *7,* 201700247-201700254.

S16. Wu, C.; Kopold, P.; Ding, Y.; Aken, P.; Maier, J.; Yu, Y. Synthesizing Porous $NaTi_2(PO_4)_3$ Nanoparticles Embedded in 3D Graphene Networks for High-Rate and Long Cycle-Life Sodium Electrodes. *ACS Nano* **2015**, *9*, 6610-6618.

S17. Yang, G.; Song, H.; Wu, M.; Wang, C. Porous $NaTi_2(PO_4)_3$ Nanocubes: A High-Rate Nonaqueous Sodium Anode Material with More Than 10000 Cycle Life. *J. Mater. Chem. A* **2015**, *3*, 18718-18726.

S18. Xu, C.; Xu, Y.; Tang, C.; Wei, Q.; Meng, J.; Huang, L.; Zhou, L.; Zhang, G.; He, L.; Mai, L. Carbon-Coated Hierarchical $NaTi_2(PO_4)_3$ Mesoporous Microflowers with Superior Sodium Storage Performance. *Nano Energy* **2016**, *28*, 224-231.

S19. Zhang, Q.; Wei, Y.; Yang, H.; Su, D.; Ma, Y.; Li, H.; Zhai, T. Tunnel-Structured K_xTiO_2 Nanorods by *In-Situ* Carbothermal Reduction as a Long Cycle and High Rate Anode for Sodium-Ion batteries. *ACS Appl. Mater. Interfaces* **2017**, *9*, 7009-7016.

S20. Zhang, Q.; Guo, Y.; Guo, K.; Zhai, T.; Li, H. Ultrafine Potassium Titanate Nanowires: A New Ti-Based Anode for Sodium Ion Batteries. *Chem. Commun.* **2016**, *52*, 6229-6232.

S21. Zou, G.; Guo, J.; Liu, X.; Zhang, Q.; Huang, G.; Fernandez, C.; Peng, Q. Hydrogenated Core-Shell MAX@ $K_2Ti_8O_{17}$ Pseudocapacitance with Ultrafast Sodium Storage and Long-Term Cycling. *Adv. Energy Mater.* **2017**, *7*, 1700700-1700708.

S22. Fu, S.; Ni, J.; Xu, Y.; Zhang, Q.; Li, L. Hydrogenation Driven Conductive $Na_2Ti_3O_7$ Nanoarrays as Robust Binder-Free Anodes for Sodium-Ion Batteries. *Nano Lett.* **2016**, *16*, 4544-4551.

S23. Dong, S.; Shen, L.; Li, H.; Pang, G.; Dou, H.; Zhang, X. Flexible Sodium-Ion Pseudocapacitors Based on 3D $Na_2Ti_3O_7$ Nanosheet Arrays/Carbon Textiles Anodes. *Adv. Funct. Mater.* **2016**, *26*, 3703-3710.

S24. Cao, K.; Jiao, L.; Pang, W.; Liu, H.; Zhou, T.; Guo, Z.; Wang, Y.; Yuan, H. $Na_2Ti_6O_{13}$ Nanorods with Dominant Large Interlayer Spacing Exposed Facet for High-Performance Na-Ion Batteries. *Small* **2016**, *12*, 2991-2997.

S25. Liao, J.; Manthiram, A. High-Performance $Na_2Ti_2O_5$ Nanowire Arrays Coated with VS_2 Nanosheets for Sodium-Ion Storage. *Nano Energy* **2015**, *18*, 20-27.

S26. Zhou, Z.; Xiao, H.; Zhang, F.; Zhang, X.; Tang, Y. Solvothermal Synthesis of $Na_2Ti_3O_7$ Nanowires Embedded in 3D Graphene Networks as an Anode for High-Performance Sodium-Ion Batteries. *Electrochim. Acta* **2016**, *211*, 430-436.

S27. Ni, J.; Fu, S.; Wu, C.; Zhao, Y.; Maier, J.; Yu, Y.; Li, L. Superior Sodium Storage in $Na_2Ti_3O_7$ Nanotube Arrays Through Surface Engineering. *Adv. Energy Mater.* **2016**, *6*, 1502568-1502575.

S28. Rudola, A.; Saravanan, K.; Devaraj, S.; Gong, H.; Balay, P. $Na_2Ti_6O_{13}$: A Potential Anode for Grid-Storage Sodium-Ion Batteries. *Chem. Commun.* **2013**, *49*, 7451-7453.

S29. Wang, X.; Li, Y.; Gao, Y.; Wang, Z.; Chen, L. Additive-Free Sodium Titanate Nanotube Array as Advanced Electrode for Sodium Ion Batteries. *Nano Energy* **2015**, *13*, 687-692.

S30. Zhang, Y.; Guo, L.; Yang, S. Three-Dimensional Spider-Web Architecture Assembled from $Na_2Ti_3O_7$ Nanotubes as a High Performance Anode for a Sodium-Ion Battery. *Chem. Commun.* **2014**, *50*, 14029-14032.

S31. Li, H.; Fei, H.; Liu, X.; Yang, J.; Wei, M. *In Situ* Synthesis of $Na_2Ti_7O_{15}$ Nanotubes on a Ti Net Substrate as a High Performance Anode for Na-Ion Batteries. *Chem. Commun.* **2015**, *51*, 9298-9300.

S32. Xie, F.; Zhang, L.; Su, D.; Jaroniec, M.; Qiao, S. $Na_2Ti_3O_7$@ N-Doped Carbon Hollow Spheres for Sodium-Ion Batteries with Excellent Rate Performance. *Adv. Mater.* **2017**, *29*, 1700989-1700994.

S33. Anwer, S.; Huang, Y.; Liu, J.; Liu, J.; Xu, M.; Wang, Z.; Chen, R.; Zhang, J.; Wu, F. Nature-Inspired $Na_2Ti_3O_7$ Nanosheets-Formed Three-Dimensional Microflowers Architecture as a High-Performance Anode Material for Rechargeable Sodium-Ion Batteries. *ACS Appl. Mater. Interfaces* **2017**, *9*, 11669-11677.

S34. Hasegawa, G.; Kanamori, K.; Kiyomura, T.; Kurata, H.; Nakanishi, K.; Abe, T. Hierarchically Porous $Li_4Ti_5O_{12}$ Anode Materials for Li and Na Ion Batteries: Effects of Nanoarchitectural Design and Temperature Dependence of the Rate Capability. *Adv. Energy Mater.* **2015**, *5*, 1400730-1400737.

S35. Yu, Z.; Song, J.; Gordin, M.; Yi, R.; Tang, D.; Wang, D. Phosphorus-Graphene Nanosheet Hybrids as Lithium-Ion Anode with Exceptional High-Temperature Cycling Stability. *Adv. Sci.* **2015**, *2,* 1400020-1400026.

S36. Park, H.; Choi, S.; Lee, S.; Cho, Y.; Hwang, G.; Song, H.; Choi, N.; Park, S. Design of an Ultra-Durable Silicon-Based Battery Anode Material with Exceptional High-Temperature Cycling Stability. *Nano Energy* **2016**, *26*, 192-199.

S37. Choi, S.; Cho, Y.; Kim, J.; Choi, N.; Song, H.; Wang, G.; Park, S. Mesoporous Germanium Anode Materials for Lithium-Ion Battery with Exceptional Cycling Stability in Wide Temperature Range. *Small* **2017**, *13*, 1603045-1603054.

S38. Racault, C.; Langlais, F.; Naslain, R. Solid-State Synthesis and Characterization of the Ternary Phase Ti_3SiC_2. *J. Mater. Sci.* **1994**, *29*, 3384-3392.